

Two-Scalar Bose-Einstein Condensates: From Stars to Galaxies

Huai-Ke Guo^a Kuver Sinha^a Chen Sun^b Joshua Swaim^c Daniel Vagie^a

^a*Department of Physics and Astronomy, University of Oklahoma, Norman, OK 73019, USA*

^b*School of Physics and Astronomy, Tel-Aviv University, Tel-Aviv 69978, Israel*

^c*Vassar College, Dept. of Physics & Astronomy, Box 745, Poughkeepsie, NY 12604*

E-mail: ghk@ou.edu, kuver.sinha@ou.edu, chensun@mail.tau.ac.il,
jswaim@vassar.edu, Daniel.d.vagie-1@ou.edu

ABSTRACT: We study the properties of Bose-Einstein Condensate (BEC) systems consisting of two scalars, focusing on both the case where the BEC is stellar scale as well as the case when it is galactic scale. After studying the stability of such systems and making contact with existing single scalar limits, we undertake a numerical study of the two interacting scalars using Einstein-Klein-Gordon (EKG) equations, including both non-gravitational self-interactions and interactions between the species. We show that the presence of extra scalars and possible interactions between them can leave unique imprints on the BEC system mass profile, especially when the system transitions from being dominated by one scalar to being dominated by the other. At stellar scales (nonlinear regime,) we observe that a repulsive interaction between the two scalars of the type $+\phi_1^2\phi_2^2$ can stabilize the BEC system and support it up to high compactness, a phenomenon only known to exist in the $+\phi^4$ system. We provide simple analytic understanding of this behavior and point out that it can lead to interesting gravitational wave signals at LIGO-Virgo. At galactic scales, on the other hand, we show that two-scalar BECs can address the scaling problem that arises when one uses ultralight dark matter mass profiles to fit observed galactic core mass profiles. In the end, we construct a particle model of two ultralight scalars with the repulsive $\phi_1^2\phi_2^2$ interaction using collective symmetry breaking. We develop a fast numerical code that utilizes the relaxation method to solve the EKG system, which can be easily generalized to multiple scalars. 

Contents

1	Introduction	1
2	Bose-Einstein Condensate with Multiple Scalars	4
2.1	Phenomenological Model	4
2.2	Metric parametrization	6
2.3	Rescaling to Dimensionless Variables	6
2.4	Time Evolution	7
2.5	Mass Profile of the BEC Structure	8
2.6	Non-Relativistic Limit	9
3	Galactic Scale BEC Structure	13
3.1	The Problem with a Single Scalar BEC	13
3.2	Two-Scalar BEC to the Rescue	14
4	Stellar Scale BEC Structure	16
4.1	Non-gravitational Interaction between Two Scalars	16
4.2	Implication for Gravitational Wave Detection	18
4.3	Comparison with previous work	20
5	Model Realization	21
6	Conclusion	22
A	Einstein Tensor	24
B	Numerical Procedure	24
B.1	Relaxation Method	24
B.2	Static Case	25
B.3	Time Evolution	27
C	Single Scalar Limit	28
D	Transitioning from Φ_1 to Φ_2 in the Nonlinear Regime	29

1 Introduction

In the last few years, there has been increasing interest in ultra-light bosonic dark matter (DM) candidates such as the axion. While the QCD axion was originally motivated by the strong CP problem [1, 2], string theory predicts a vast landscape of axion-like particles (ALPs) [3–6] with

masses across several orders of magnitude and a rich phenomenology. Studies of sub-eV (pseudo-) scalars as DM candidates have yielded interesting signals and novel proposals for direct detection experiments [7–11], to name a few.

In particular, due to its bosonic nature, ultra-light bosonic DM can exhibit collective behaviors at the macroscopic level that are not obvious at the Lagrangian level. It has been observed and well understood in condensed matter physics that for bosons there exists a unique phase, the Bose-Einstein Condensate (BEC) phase, once the ensemble is cooled down below the critical temperature. Given the abundance of the DM population, this translates the requirement of the occupancy number $n > (mv)^3$ to an upper bound of the scalar mass, $m < \text{eV}$ [12]. The maximal mass of the BEC object can be crudely estimated as $M \lesssim M_{Pl}^2/m$ [13]. This singles out two scales of particular interest to the community: galactic scale BEC with $m \sim 10^{-22}$ eV, and stellar scale BEC with $m \sim 10^{-10}$ eV.

On galactic scales, condensates of ultralight bosons have been shown to produce core like halos by quantum pressure [14–19], with various studies on its constraints [20–24]. A good understanding of the theoretical mass profile of such a BEC system not only provides insights on the particle nature of DM, but could also have implications for quasar lensing time delay and the recent Hubble tension [25]. On smaller scales, such BEC systems can form stellar scale structures dubbed boson stars [26, 27], with scalars free from interaction [28], with attractive ϕ^4 interaction [29–37], repulsive ϕ^4 interaction [13, 38, 39], and repulsive $\cos(\phi/f)$ potential [12, 40]. A few variations such as multistate boson stars from generic scalars have also been explored, in an attempt to reproduce realistic models of DM halos [41]. BEC states with angular momentum is studied in a recent work [42]. New ways of probing BEC systems at different scales include using Big Bang Nucleosynthesis (BBN) [43], galaxy rotation curves [23, 44], gravitational wave (GW) from binary boson star mergers [40, 45], GW from BEC collisions [46], speed of GWs passing through BEC [47], electromagnetic emission [48–50], GW from extreme mass ratio inspiral systems [51], and optical lensing [52].

Many studies have been dedicated to understanding the map between properties at the Lagrangian level and the behavior of the BEC system such as its mass and density profile [12, 24, 29–31, 34–38, 40, 53–55]. In [56], hydrodynamic approach is used and confirms the results from field space analysis. In [57], formation of boson stars inside DM halo is simulated. On the other hand, the effect of extra scalars in a BEC system with both gravitational and possibly non-gravitational interactions among the scalars remains largely under-explored. In particular, due to numerical challenges, most previous studies have focused on single scalar BEC systems, with a few exceptions: multiple scalar BEC systems with negligible non-gravitational interactions were explored in [58]; analytical approximations for multi-scalar BEC systems with self-interactions were explored in [59]; a Newtonian analysis on multi-scalar BEC in the limit of large quartic coupling [60]. Existence of solutions in the presence of a few types of interactions are studied in [61–63]. In contrast, we undertake a full General Relativity (GR) numerical study of the properties of BECs made of two interacting scalars, including both non-gravitational self-interactions and interactions between the scalars, followed by simple analytical understanding, and its phenomenological implications. Given that feeble repulsive self-interactions can lead to drastic changes in the mass profile at the macroscopic level [13, 40], it can be expected that interactions between different scalars will have an important impact and leave unique imprints on the BEC system mass profile. The purpose of

our paper is to carefully investigate such imprints, and ask whether they can be utilized to predict unique observational signatures or help address long-standing puzzles.

Our study proceeds along two directions. At the stellar scale, a light scalar of mass $m \sim 10^{-10}$ eV allows the formation of solar mass stellar structures. The formation and compactness can be greatly enhanced due to the presence of a repulsive self-interaction in the scalar potential, or compromised by an attractive self-interaction [26, 29, 40]. The strength and form of the non-gravitational interactions leave imprints on the GW signal. With the presence of extra scalars and interactions between multiple scalars, the features in GW are richer, with the maximal compactness of a stable BEC system being $\sim \mathcal{O}(0.2)$. In particular, we show the important role the interaction between the species $(\pm\phi_1^2\phi_2^2)$ plays in either stabilizing or destabilizing the self-gravitating two scalar BEC system. It could also have implications for the recent GW190521 event. With this perspective in mind, we explore the mass versus compactness parameter space of a stellar BEC consisting of two ultralight scalars.

The second major focus of our paper is the behavior of the BEC at galactic scales. In the case of BEC DM composed of a single scalar field, the mass profile has a unique scaling behavior controlled by a single parameter: the central value of the wave function (\propto (central density)^{1/2} of the BEC.) As shown in [23, 24], this scaling behavior is in tension with observational data [64]. This can be understood from the scaling behavior of the scalar’s equation of motion, either from the Schrödinger-Newton equation, or from the relativistic EKG equation: in the single scalar case, the scaling is parametrized as $M[\phi(0)], R[\phi(0)]$, with $\phi(0)$ being the central value of the classical wave function. This means that dynamics does not play any role in determining the mass-radius relation, $M(R)$, which is fixed once a scalar potential is chosen. With the presence of a second scalar, the theory space is enlarged from one dimensional $\{\phi(0)\}$ to two dimensional $\{\phi_1(0), \phi_2(0)\}$. As we will show in subsequent sections, the ratio of the two BEC structures plays a role in the mass-radius relation of the total BEC structure, meanwhile the system is stable against radial perturbation even the fraction of each component varies. This holds out the possibility of accommodating observational data with BEC DM composed of multiple scalars while maintaining stability against radial perturbation; we show that this is indeed the case. We stress that, we are not claiming to provide a mass-radius relation of the BEC, as that requires accounting for the dynamics of the scalars that determines the mass ratio of the two components, which is beyond the scope of this work. Instead, we study the stability of the BEC against radial perturbations, when a ratio of the two components is given. Under this assumption, we show that there is parameter space to accommodate the galactic data [64] and address the problem raised by [24]. As the first part of a study series, we lay out the ground work and justifies the necessities of studying multi-scalar ultralight dark matter dynamics.

Our results rely on numerically integrating the complete relativistic Einstein-Klein-Gordon (EKG) equations. We do so by implementing an efficient algorithm not common in boson star studies to solve the set of equation of motion for arbitrary parameters. Our algorithm employs the Relaxation Method described in [65] which can solve a system of differential equations subjected to their boundary conditions as opposed to the initial value shooting method typically used in these type of equations. This approach can be easily extended to N-scalar systems.¹ The results are

¹We note that the relaxation method avoids the problem of multi-dimension shooting, yet it still suffers from the

verified by comparing against the usual shooting method in the single scalar case [40, 51]. Besides the exact numerical solutions, we also provide analysis adopting a simple ansatz and write out the non-relativistic Hamiltonian. The scaling behavior in the linear regime is affected mainly by the mass ratio (m_1/m_2) of the two scalars, while that in the nonlinear regime is affected more by the non-gravitational interactions between the two scalars. In particular, we demonstrate that with mild repulsive interactions between the two scalars $\lambda_{12}\phi_1^2\phi_2^2$, the system can be stabilized up to very large density, a behavior that was only known to exist in the case of repulsive self-interaction $\lambda\phi^4$ [13, 29, 38, 40]. We show that such a repulsive interaction can be realized in a realistic particle model with collective symmetry breaking [66].

To summarize, we highlight the following points in this work:

- At the galactic scale, we show that the presence of a second scalar renders the theory capable of accommodating the mass profile indicated by observational data while maintaining its radial stability, which cannot be done in a system of a single scalar [24].
- At the stellar scale, we show that a repulsive interaction between two scalars, $\lambda\phi_1^2\phi_2^2$, can stabilize the system up to high density, which was only known to exist in a single scalar system with repulsive self-interactions [13, 38, 40, 51]. We provide a particle model realization as a proof of concept.
- We have developed complete and fast code that utilizes the Relaxation Method to solve the BEC system with two scalars, and is easy to generalize to multiple scalars. The code has been made public.²

This paper is organized as follows. We will begin by defining the phenomenological model of two scalars in Section 2. We set up the stage for numerical computations of the Einstein-Klein-Gordon system. We then take the non-relativistic limit to simplify the system and perform analytical investigations of the behavior, including both the transition from one scalar dominating to the other, and the effect of the non-gravitational interactions between the two scalars. We then verify the static solutions numerically, as well as perform time evolution of the system to ensure that the solution is indeed stable against radial perturbations. In Section 3 we apply our analysis toolkit to the galactic scale BEC system and show that this can address the scaling problem of ultralight dark matter while maintaining radial stability. In Section 4 we focus on the stellar scale and show the effect of non-gravitational interactions in the context of two scalar system. In Section 5 we discuss a possible particle model construction. We then conclude in Section 6. We provide details for computing the equation of motion in Appendix A, outline the numerical recipe we use for the code in Appendix B, and verify that it can reproduce the single scalar limit in Appendix C.

2 Bose-Einstein Condensate with Multiple Scalars

2.1 Phenomenological Model

The Lagrangian for a complex scalar system consisting of N particles reads

stiffness issue if the separation of scales is large. That means, in the case of N -scalars, the separation between the lightest one and the heaviest one cannot be too large.

²The code can be downloaded at <https://github.com/vagiedd/BosonStars> .

$$\mathcal{L} = \sum_n^N -\frac{1}{2}g^{\mu\nu}\partial_\mu\phi_i^*\partial_\nu\phi_i - V(|\phi_1|^2, |\phi_2|^2, \dots) \quad (2.1)$$

where $g^{\mu\nu}$ is the space-time metric inverse with the signature $(-, +, +, +)$, and ϕ_n is the n -th scalar field. The potential V characterizes the interactions between the scalar fields and is a function of the coupling strengths and the modulus squared of ϕ . In this work we only consider the case of two complex scalars in the ground state, which can be easily generalized to compute BEC of more scalar fields in our numerical framework. The Lagrangian for 2 complex scalars with generic interactions reads

$$\begin{aligned} \mathcal{L} = & -\frac{1}{2}g^{\mu\nu}\partial_\mu\phi_1^*\partial_\nu\phi_1 - \frac{1}{2}m_1^2|\phi_1|^2 - \frac{1}{4}c_1|\phi_1|^4 \\ & -\frac{1}{2}g^{\mu\nu}\partial_\mu\phi_2^*\partial_\nu\phi_2 - \frac{1}{2}m_2^2|\phi_2|^2 - \frac{1}{4}c_2|\phi_2|^4 - \frac{1}{4}c_{12}|\phi_1|^2|\phi_2|^2, \end{aligned} \quad (2.2)$$

where c' s are the coupling constants that can be either positive or negative. We note that stability of the potential is ensured by some higher order operators and this is taken as a truncation of the full potential. The scalar fields interact with gravity through the the minimal gravitational coupling

$$S = \int \left(\frac{1}{16\pi G}R + \mathcal{L} \right) \sqrt{-g}d^4x, \quad (2.3)$$

where R is the Ricci scalar determined by the metric g and \mathcal{L} is given in Eq. 2.2. Variation of the action with respect to the metric gives rise to Einstein equations

$$R_{\mu\nu} - \frac{1}{2}R = 8\pi GT_{\mu\nu}, \quad (2.4)$$

where $R_{\mu\nu}$ is the Ricci tensor, and $T_{\mu\nu}$ the energy-momentum tensor given by

$$\begin{aligned} T_\mu^\nu = & \sum_i \left(\frac{\delta\mathcal{L}}{\delta(\partial_\nu\phi_i)}\partial_\mu\phi_i + \frac{\delta\mathcal{L}}{\delta(\partial_\nu\phi_i^*)}\partial_\mu\phi_i^* \right) - \delta_\mu^\nu\mathcal{L} \\ = & -\frac{1}{2}g^{\nu\nu'}\partial_{\nu'}\phi_1^*\partial_\mu\phi_1 - \frac{1}{2}g^{\nu\nu'}\partial_{\nu'}\phi_1\partial_\mu\phi_1^* - \frac{1}{2}g^{\nu\nu'}\partial_{\nu'}\phi_2^*\partial_\mu\phi_2 \\ & - \frac{1}{2}g^{\nu\nu'}\partial_{\nu'}\phi_2\partial_\mu\phi_2^* + \delta_\mu^\nu \left(\frac{1}{2}g^{\mu\mu'}\partial_{\mu'}\phi_1^*\partial_{\nu'}\phi_1 + \frac{1}{2}m_1^2|\phi_1|^2 + \frac{1}{4}c_1|\phi_1|^4 \right. \\ & \left. + \frac{1}{2}g^{\mu\mu'}\partial_{\mu'}\phi_2^*\partial_{\nu'}\phi_2 + \frac{1}{2}m_2^2|\phi_2|^2 + \frac{1}{4}c_2|\phi_2|^4 + \frac{1}{4}c_{12}|\phi_1|^2|\phi_2|^2 \right). \end{aligned} \quad (2.5)$$

Note that since gauge fields are not the focus here, the simpler definition of T_μ^ν is equivalent to the one using variation with respect to the metric. If we vary the action with respect to the scalar field we get the Klein-Gordon equation

$$g^{\mu\nu}\nabla_\mu\nabla_\nu\phi_i = \frac{dV}{d\phi_i^*}, \quad (2.6)$$

where ∇ is the covariant derivative that contains the Christoffel symbols.

2.2 Metric parametrization

Assuming spherical symmetry of the metric, we parametrize the metric as

$$ds^2 = -B(r)dt^2 + A(r)dr^2 + r^2d\theta^2 + r^2\sin^2\theta d\phi^2. \quad (2.7)$$

Solving the t and r components of the Einstein equation, we have

$$\begin{aligned} & \frac{4\pi G_N}{B(r)}\partial_t\phi_1\partial_t\phi_1^* + \frac{4\pi G_N}{A(r)}\partial_r\phi\partial_r\phi_1^* + \frac{4\pi G_N}{B(r)}\partial_t\phi_2\partial_t\phi_2^* + \frac{4\pi G_N}{A(r)}\partial_r\phi_2\partial_r\phi_2^* \\ & + 4\pi G_N m_1^2|\phi_1|^2 + 4\pi G_N m_2^2|\phi_2|^2 + 2\pi G_N c_1|\phi_1|^4 + 2\pi G_N c_2|\phi_2|^4 + 2\pi G_N c_{12}|\phi_1|^2|\phi_2|^2 \\ & - \frac{A'(r)}{rA(r)^2} + \frac{1}{r^2A(r)} - \frac{1}{r^2} = 0, \\ & \frac{4\pi G_N}{B(r)}\partial_t\phi_1\partial_t\phi_1^* + \frac{4\pi G_N}{A(r)}\partial_r\phi_1\partial_r\phi_1^* + \frac{4\pi G_N}{B(r)}\partial_t\phi_2\partial_t\phi_2^* + \frac{4\pi G_N}{A(r)}\partial_r\phi_2\partial_r\phi_2^* \\ & - 4\pi G_N m_1^2|\phi_1|^2 - 4\pi G_N m_2^2|\phi_2|^2 - 2\pi G_N c_1|\phi_1|^4 - 2\pi G_N c_2|\phi_2|^4 - 2\pi G_N c_{12}|\phi_1|^2|\phi_2|^2 \\ & - \frac{B'(r)}{rA(r)B(r)} - \frac{1}{r^2A(r)} + \frac{1}{r^2} = 0. \end{aligned} \quad (2.8)$$

Two extra constraints come from the Klein-Gordon equations of motion. Plugging in the covariant derivative, we get

$$\begin{aligned} & \frac{1}{A}\partial_r^2\phi_1 - \frac{1}{B}\partial_t^2\phi_1 + \partial_r\phi_1 \left(\frac{B'(r)}{2A(r)B(r)} - \frac{A'(r)}{2A(r)^2} + \frac{2}{A(r)r} \right) \\ & - m_1^2\phi_1 - c_1|\phi_1|^2\phi_1 - \frac{1}{2}c_{12}|\phi_2|^2\phi_1 = 0, \\ & \frac{1}{A}\partial_r^2\phi_2 - \frac{1}{B}\partial_t^2\phi_2 + \partial_r\phi_2 \left(\frac{B'(r)}{2A(r)B(r)} - \frac{A'(r)}{2A(r)^2} + \frac{2}{A(r)r} \right) \\ & - m_2^2\phi_2 - c_2|\phi_2|^2\phi_2 - \frac{1}{2}c_{12}|\phi_1|^2\phi_2 = 0. \end{aligned} \quad (2.9)$$

2.3 Rescaling to Dimensionless Variables

We take the harmonic ansatz with energy eigenstates $\phi_i(t, r) = \Phi_i(r)e^{-i\mu_i t}$. Plugging it into the equation of motion we can separate the time evolution part of ϕ_i . In order to solve it numerically, we perform the following rescaling of variables:

$$\begin{aligned} \Phi_1 &= \tilde{\Phi}_1 (4\pi G_N)^{-1/2}, & \Phi_2 &= \tilde{\Phi}_2 (4\pi G_N)^{-1/2}, \\ \mu_1 &= \tilde{\mu}_1 m_1, & \mu_2 &= \tilde{\mu}_2 m_1, \\ c_1 &= \tilde{\lambda}_1 4\pi G_N m_1^2, & c_2 &= \tilde{\lambda}_2 4\pi G_N m_1^2, \\ c_{12} &= \tilde{\lambda}_{12} 4\pi G_N m_1^2, & m_2 &= \tilde{m}_r m_1, \\ r &= \tilde{r}/m_1, \end{aligned} \quad (2.10)$$

where the variable with a tilde is dimensionless.³ If one parametrizes c_i in the notation usually adapted in the axion literature using the Peccei-Quinn symmetry breaking scale, $c_i = m_i^2/f_i^2$, it

³For comparison, in Ref. [13], $\tilde{r}, \tilde{\Phi}, \tilde{\mu}, \tilde{\lambda}$ are denoted as $x, \sigma, \Omega, \Lambda$ respectively.

reads

$$\begin{aligned}\tilde{\lambda}_1 &= \frac{1}{4\pi} \left(\frac{M_{Pl}}{f_1} \right)^2, \\ \tilde{\lambda}_2 &= \frac{1}{4\pi} \left(\frac{M_{Pl}}{f_2} \right)^2 \tilde{m}_r^2.\end{aligned}\tag{2.11}$$

The strength of the interaction terms can be parameterized by the size of f_i . In other words, $\tilde{\lambda} \sim 1$ parametrizes a self-interaction whose strength is comparable to gravity with $f \sim M_{Pl}$. The dimensionless variables will be used for numerically solving the system. In what follows, we assume m_1, m_2 close to each other, so are f_1 and f_2 . Therefore, we parametrize the coupling strength c 's in the unit of m_1^2/f^2 with f chosen at 10^{17} GeV. In other words, we have

$$\begin{aligned}c_1 &= \lambda_1 \frac{m_1^2}{f^2}, \\ c_2 &= \lambda_2 \frac{m_1^2}{f^2}, \\ c_{12} &= \lambda_{12} \frac{m_1^2}{f^2}.\end{aligned}\tag{2.12}$$

We will parametrize the three physical couplings with order one numbers in a tuple, $(\lambda_1, \lambda_2, \lambda_{12})$ in the rest of the paper. In terms of the dimensionless variables, we can write the equations of motion as

$$\begin{aligned}& \left(\frac{\tilde{\mu}_1^2}{B} + 1 \right) \tilde{\Phi}_1^2 + \frac{1}{A} \tilde{\Phi}_1'^2 + \frac{1}{2} \tilde{\lambda}_1 \tilde{\Phi}_1^4 + \left(\frac{\tilde{\mu}_2^2}{B} + \tilde{m}_r^2 \right) \tilde{\Phi}_2^2 + \frac{1}{A} \tilde{\Phi}_2'^2 + \frac{1}{2} \tilde{\lambda}_2 \tilde{\Phi}_2^4 + \frac{1}{2} \tilde{\lambda}_{12} \tilde{\Phi}_1^2 \tilde{\Phi}_2^2 \\ & - \frac{A'}{\tilde{r} A^2} + \frac{1}{\tilde{r}^2 A} - \frac{1}{\tilde{r}^2} = 0, \\ & \left(\frac{\tilde{\mu}_1^2}{B} - 1 \right) \tilde{\Phi}_1^2 + \frac{1}{A} \tilde{\Phi}_1'^2 - \frac{1}{2} \tilde{\lambda}_1 \tilde{\Phi}_1^4 + \left(\frac{\tilde{\mu}_2^2}{B} - \tilde{m}_r^2 \right) \tilde{\Phi}_2^2 + \frac{1}{A} \tilde{\Phi}_2'^2 - \frac{1}{2} \tilde{\lambda}_2 \tilde{\Phi}_2^4 - \frac{1}{2} \tilde{\lambda}_{12} \tilde{\Phi}_1^2 \tilde{\Phi}_2^2 \\ & - \frac{B'}{\tilde{r} AB} - \frac{1}{\tilde{r}^2 A} + \frac{1}{\tilde{r}^2} = 0, \\ & \frac{1}{A} \tilde{\Phi}_1'' + \left(\frac{\tilde{\mu}_1^2}{B} - 1 \right) \tilde{\Phi}_1 + \tilde{\Phi}_1' \left(\frac{B'}{2AB} - \frac{A'}{2A^2} + \frac{2}{A\tilde{r}} \right) - \tilde{\lambda}_1 \tilde{\Phi}_1^3 - \frac{1}{2} \tilde{\lambda}_{12} \tilde{\Phi}_2^2 \tilde{\Phi}_1 = 0, \\ & \frac{1}{A} \tilde{\Phi}_2'' + \left(\frac{\tilde{\mu}_2^2}{B} - \tilde{m}_r^2 \right) \tilde{\Phi}_2 + \tilde{\Phi}_2' \left(\frac{B'}{2AB} - \frac{A'}{2A^2} + \frac{2}{A\tilde{r}} \right) - \tilde{\lambda}_2 \tilde{\Phi}_2^3 - \frac{1}{2} \tilde{\lambda}_{12} \tilde{\Phi}_1^2 \tilde{\Phi}_2 = 0.\end{aligned}\tag{2.13}$$

This concludes our setup of the problem, and we can solve Eq. (2.13) numerically. For details of the numerical algorithm, one can refer to Appendix B. Before we proceed to discuss the results and physical implications, we take a small detour to discuss the stability of solutions to Eq. (2.13).

2.4 Time Evolution

To verify that the solution is indeed stable against radial perturbations, we perform the time evolution using a finite difference method. This way, we can verify the temporal harmonic ansatz $\Phi_i(r, t) = \Phi_i(r) e^{-i\mu_i t}$. The detailed procedure can be found in Appendix B.3. We outline this procedure here briefly.

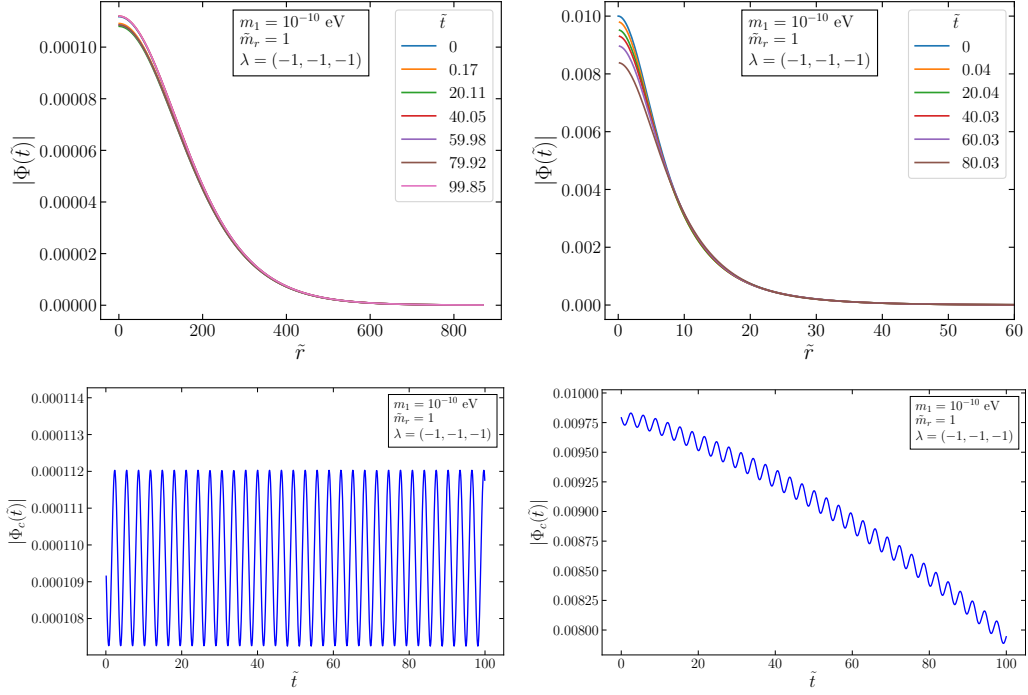


Figure 1: From top left clockwise: 1) time snapshots of the wave function of a stable configuration being radially perturbed $\psi \rightarrow \psi(1 + \epsilon)$, with the vertical axis showing the sum of the modulus squared of the wave functions for Φ_1 and Φ_2 for $\lambda_1 = \lambda_2 = \lambda_{12} = -1$. 2) Same plot for an unstable configuration by increasing the central density controlled by $\Phi_1(0)$ and $\Phi_2(0)$. The wave function diverges quickly after a short time. 3) Unstable configuration in time domain shows the BEC collapsing within a short time period. 4) Stable configuration in time domain shows the system having small oscillation but maintaining a stable configuration. All the radial perturbations are done with $\epsilon \sim 2\%$. The stable configuration is chosen as $\tilde{\Phi}_1(0) = 10^{-4}$ and $\tilde{\Phi}_2(0) = 5 \times 10^{-5}$; the unstable configuration $\tilde{\Phi}_1(0) = 10^{-4}$ and $\tilde{\Phi}_2(0) = 10^{-2}$.

First, one solves the static equations (2.13). This will serve as the initial condition for the numerical time evolution. To check if it is a stable system, we perform a radial perturbation by $\Phi \rightarrow \Phi(1 + \epsilon)$, and use $\Phi(1 + \epsilon)$ as the initial condition instead. Here ϵ represents how far we perturb away from the static solution. In the stable case, the system can evolve for a long time with small oscillations, while in the unstable case the wave function quickly collapses or blows up depending on the sign of ϵ . We show a sample stable solution in Fig. 1 for $\lambda_1 = \lambda_2 = \lambda_{12} = -1$ and initial central densities of $\tilde{\Phi}_1(0) = 10^{-4}$ and $\tilde{\Phi}_2(0) = 5 \times 10^{-5}$, together with an unstable solution of $\tilde{\Phi}_1(0) = 10^{-4}$ and $\tilde{\Phi}_2(0) = 10^{-2}$. On top of the quasi-normal mode, there is no sign of decay after $\sim 100m^{-1}$ in the stable scenario while the field with the unstable configuration decays considerably.

2.5 Mass Profile of the BEC Structure

With the solution to Eq. (2.13) in hand, one can derive the physical properties of the BEC system. The total mass of the BEC system is found by integrating the T_0^0 component of the energy

momentum tensor

$$\begin{aligned}
M_{BS} &\equiv 4\pi \int_0^\infty dr r^2 T_0^0 \\
&= 4\pi \int_0^\infty dr r^2 \left(\frac{\mu_1^2}{2B} \Phi_1^2 + \frac{1}{2} m_1^2 \Phi_1^2 + \frac{1}{2A} \partial_r \Phi_1^2 + \frac{1}{4} \lambda_1 \Phi_1^4 + \right. \\
&\quad \left. \frac{\mu_2^2}{2B} \Phi_2^2 + \frac{1}{2} m_2^2 \Phi_2^2 + \frac{1}{2A} \partial_r \Phi_2^2 + \frac{1}{4} \lambda_2 \Phi_2^4 + \frac{1}{4} \lambda_{12} \Phi_1^2 \Phi_2^2 \right). \quad (2.14)
\end{aligned}$$

In the linear regime, *i.e.* non-relativistic limit, this reduces to the sum of the rest mass from the two scalars: $M_{BS} \approx M_1 + M_2 = m_1 N_1 + m_2 N_2 + \mathcal{O}(B-1) + \mathcal{O}(1-A)$, with the subscript BS standing for BEC system. The compactness of the BEC system is defined as the mass-radius ratio in natural units

$$C_{BS} = \frac{G_N M_{BS}}{R_{90}} \quad (2.15)$$

where R_{90} is the radius that contains 90% of the total mass. Similar to the mass components, in the limit of small interaction between Φ_1 and Φ_2 , we can also define C_1 and C_2 as the compactness of the BEC component corresponding to Φ_1 and Φ_2 , respectively. For a given set of model parameters, (λ, m) , in the single scalar scenario, the mass and compactness are solely determined by a single variable, $\Phi(r=0)$, which is related to the central density of the BEC system. As a result, the compactness is a function of mass. In the case of two scalar BEC, this is no longer true. One can find solutions with different combinations of $\Phi_1(0)$, $\Phi_2(0)$, which essentially enlarges the parameter space to being 2-dimensional. The mass profile in the $C_{BS} - M_{BS}$ plane is no longer a curve, but a 2D region. A detailed analysis for various BEC mass profiles will be given in the results section of Section 3 and 4 respectively.

2.6 Non-Relativistic Limit

Although we solve the system in the full relativistic regime, expanding in the weak gravity limit can bring insights to various properties of the system. The waveforms of Φ_1 and Φ_2 should decay to zero as $r \rightarrow \infty$. We also expect that the metric becomes non-relativistic for large r such that

$$\begin{aligned}
A(r) &= 1 - 2V(r) \\
B(r) &= 1 + 2V(r) \\
V(r) &= -\frac{GM(r)}{r} = -\frac{G(M_1(r) + M_2(r))}{r}. \quad (2.16)
\end{aligned}$$

We adopt the following ansatz for the wave function, which is verified by the numerical computation to hold well enough at sufficiently large radius.

$$\Phi_i = \sqrt{\frac{N_i}{\pi m_i R_i^3}} e^{-r/R_i} \quad (2.17)$$

where N_i is the total number of particles for either Φ_1 or Φ_2 and R_i is characteristic size of each BEC clump. Using this non-relativistic ansatz, we may integrate each term individually in Eq. 2.14

and combine terms to give the non-relativistic Hamiltonian. In the weak gravity limit, one can parametrize the eigenvalues as

$$\mu_i = m_i (1 - \alpha V(r)). \quad (2.18)$$

Matching to the non-relativistic results in the leading terms, we found $\alpha = 5/4$ reproduces the self-gravity term as in the single scalar case [40]. We can then write out the Hamiltonian as

$$\begin{aligned} H_{kin} &= + \frac{N_1}{2m_1 R_1^2} + \frac{N_2}{2m_2 R_2^2} \\ H_{int} &= + \frac{\lambda_1 N_1^2}{32\pi f^2 R_1^3} + \frac{\lambda_2 N_2^2}{32\pi f^2 R_2^3} + \frac{\lambda_{12} N_1 N_2}{4\pi f^2 (R_1 + R_2)^3} \\ H_{grav} &= - \frac{5Gm_1^2 N_1^2}{16R_1} - \frac{5Gm_2^2 N_2^2}{16R_2} - \frac{Gm_1 m_2 N_1 N_2}{R_{\text{eff}}} \\ H_{metric} &= - \frac{5GN_1^2}{16R_1^3} - \frac{5GN_2^2}{16R_2^3} - \frac{GN_1 N_2}{\tilde{R}_{\text{eff}}^3} \end{aligned} \quad (2.19)$$

with

$$\begin{aligned} \frac{1}{R_{\text{eff}}} &= \frac{5}{8R_1} + \frac{5}{8R_2} - \frac{1}{R_1 + R_2} - \frac{R_1 R_2}{(R_1 + R_2)^3}, \\ \frac{1}{\tilde{R}_{\text{eff}}^3} &= \frac{m_1(4R_1 + R_2)}{m_2(R_1 + R_2)^4} + \frac{m_2(R_1 + 4R_2)}{m_1(R_1 + R_2)^4}. \end{aligned}$$

We can immediately recognize the familiar form of kinetic terms, self-interaction terms, self-gravity terms, and the first two terms in H_{metric} , which are due to the kinetic term in the curved space-time consistent with the result in [40, 51]. However, the Hamiltonian also contains a term proportional to $\lambda_{12} N_1 N_2$ that is due to the non-gravitational interaction between the two scalars. In addition, there are terms proportional to $G_N M_1 M_2$ due to the gravitational interaction between the two scalars which are not present in the single scalar case. One recovers the one scalar result if either N_1 or N_2 is set to zero. In the limit of $\lambda_{12} \rightarrow 0$ and $R_1, R_2 \sim R$, $1/R_{\text{eff}}$ reduces to $(5/8R)$, which is consistent with the result of [59] up to the H_{grav} term.

A discussion based on the Hamiltonian is in order. In the linear regime, one can safely neglect the terms in H_{int} and H_{metric} . Without loss of generality, when $N_1 \gg N_2$, the gradient term will balance the gravity term Eq. 2.19 to give

$$N \approx N_1 \propto \frac{M_{Pl}^2}{m_1^3 R_1}. \quad (2.20)$$

Whether Φ_1 or Φ_2 dominates is solely determined by the central value, $\Phi_1(0)$ and $\Phi_2(0)$. Therefore, we have

$$M_{BS} \sim \begin{cases} \frac{M_{Pl}^2}{m_1} \sqrt{C}, & N_1 \gg N_2 \\ \frac{M_{Pl}^2}{m_2} \sqrt{C}, & N_2 \gg N_1 \end{cases} \quad (2.21)$$

It is expected that when one goes from the Φ_1 -dominating regime to Φ_2 -dominating regime, the $M - C$ relation will smoothly transition from one to the other. This is verified by the numerical

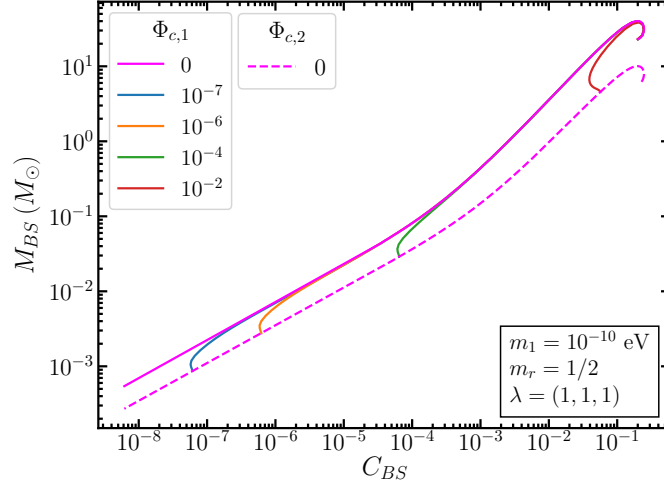


Figure 2: The total mass vs compactness for various values of $\Phi_1(0)$ and $\Phi_2(0)$ with $\lambda_1 = 1$, $\lambda_2 = 1$, and $\lambda_{12} = 1$. We scan $\Phi_1(0)$ and $\Phi_2(0)$ to show the existence of stable solutions. The solid magenta line corresponds to the single scalar limit with $m = 5 \times 10^{-11}$ eV and the dashed magenta line is the single scalar limit with $m = 10^{-10}$ eV. The solid lines in between corresponds to $m_1 = 10^{-10}$ eV and $m_2 = 5 \times 10^{-11}$ with each curve corresponding to a different fixed $\Phi_1(0)$ and scanning over $\Phi_2(0)$. We let Φ_1 dominate first, and Φ_2 starts to dominate the system at different places due to $\Phi_1(0)$ fixed at different values in blue, orange, green, and red curves. One can see that the moment Φ_2 starts to dominate, the curve transition from the dashed to solid magenta as expected.

computation and shown in Fig. 2. This has interesting implications for the solitonic core, in the context of galactic scale BEC. We will discuss this feature in more detail in Section 3. Note that we only show the result with $m_2/m_1 = 1/2$ due to the numerical complexity, but in principle the result should hold for much larger scalar ratios. This means that by adjusting the central densities of the two BEC components, $\Phi_1(0)$ and $\Phi_2(0)$, one can have non-trivial mass profiles that cannot be mimicked by a single scalar BEC system.

In the nonlinear regime, the non-gravitational interactions are important. In contrast to the single scalar case, we have three non-gravitational interaction terms proportional to λ_1 , λ_2 , and λ_{12} respectively. It is known that a repulsive self-interaction $+\Phi^4$ stabilizes the system [13, 29, 38, 40, 51], while the attractive $-\Phi^4$ renders the system unstable once it goes to the nonlinear regime [29, 37, 40]. In the two scalar system, we observe that a repulsive non-gravitational interaction $+\Phi_1^2\Phi_2^2$ also stabilizes the system. This can be understood by looking into the Hamiltonian of the system. In the nonlinear regime, the important terms are the gravity potential and the nonlinear terms. We assume Φ_2 dominates the system, $N_2 > N_1$:

$$\tilde{H}(R_2) \approx \frac{\tilde{\lambda}_2 \tilde{N}_2^2}{8\tilde{R}_2^3} + \frac{\tilde{\lambda}_{12} \tilde{N}_2 \tilde{N}_1}{8\tilde{R}_2^3} - \frac{5\tilde{N}_2^2}{16\tilde{R}_2}, \quad (2.22)$$

where $H = \tilde{H}m\Delta^2$, $N = \tilde{N}(m/M_{Pl})^2\Delta$, with Δ being some large number for normalization. If we start with $\tilde{\lambda}_1 < 0$, $\tilde{\lambda}_2 < 0$, $\tilde{\lambda}_{12} > 0$ ($\tilde{\lambda}_1 > 0$, $\tilde{\lambda}_2 > 0$, $\tilde{\lambda}_{12} < 0$), we observe that the BEC system

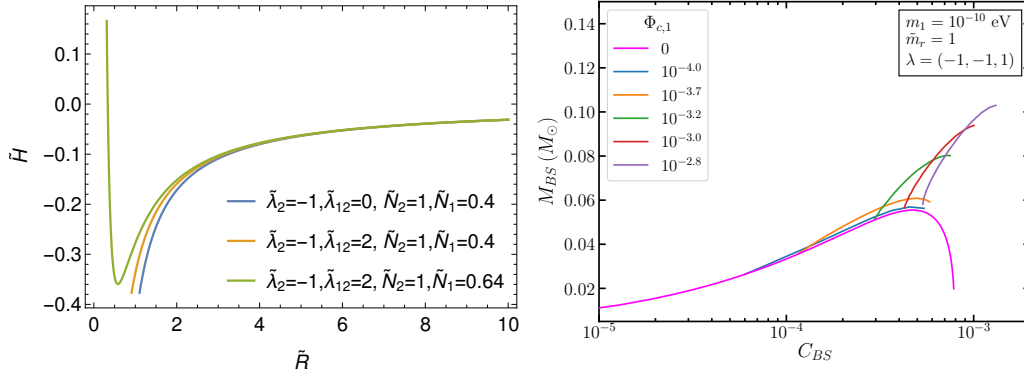


Figure 3: Left: the rescaled Hamiltonian as a function of the BEC radius \tilde{R} in the nonlinear regime, and $N_2 > N_1$. In particular, we observe that when there is no interaction between Φ_1 and Φ_2 , it behaves the same as the single scalar case where $-\Phi_2^4$ destroys the local minimum so the system is not stable (blue curve). When (a) there is a repulsive interaction $\lambda_{12} > 0$, and (b) the sub-dominant scalar number, N_1 , is large enough, one can see the local minimum is restored (green curve). This happens only when both conditions are fulfilled. With only (a), the system still lacks local minimum (orange curve). Right: The numerical solutions verifies the previous analysis. As an example, we choose $\tilde{\lambda}_1 = 1, \tilde{\lambda}_2 = -1, \tilde{\lambda}_{12} = 1$. All curves are generated by scanning over $\Phi_2(0)$. The magenta curve is with only Φ_2 field. One can see there are no more solutions beyond $C_{BS} \gtrsim 8 \times 10^{-4}$ due to $-\Phi_2^4$ self-interaction. In the colored curves we add a sub-component Φ_1 with $\Phi_1(0)$ fixed to the labeled value, and again scan over $\Phi_2(0)$. When the subdominant scalar Φ_1 number is large enough (green, red, purple), the system can become stable again and one can find solutions at $C_{BS} > 10^{-3}$, consistent with our analytical approximation. We scan $\Phi_2(0)$ to show the existence of stable solutions.

can be stabilized (destabilized), respectively, when the following condition is met:

$$\frac{\tilde{N}_1}{\tilde{N}_2} > \left| \frac{\tilde{\lambda}_2}{\tilde{\lambda}_{12}} \right|. \quad (2.23)$$

We demonstrate this both analytically and numerically in Fig. 3. This has some interesting implications for boson stars. Contrary to the common understanding that BECs resulting from $-\phi^4$ or $\Lambda^4(1 - \cos(\phi))$ potentials (e.g. axion stars) are dilute, they can be stabilized up to high density if there are multiple of them and different species interact with each other through a repulsive interaction.

In other combinations of λ 's, the presence of the coupling between the two scalars can also offer unique features in the $C_{BS} - M_{BS}$ curves in the non-linear regime that are not possible in the single scalar limit. This has interesting implications for the stellar scale BEC structure. We will discuss this application in more detail in Section 4 and show the results for how the nonlinear regime is changed by varying the model parameters, $\lambda_1, \lambda_2, \lambda_{12}$, and m_1, m_2 .

3 Galactic Scale BEC Structure

Having discussed the behavior of the two scalar BEC system, we now turn to applications: the first being the implications at galactic scales. We first briefly review the problem of using single scalar BEC to fit galaxy data. For details one can refer to e.g. [24]. We then show that with the second scalar and the transitioning behavior demonstrated in Section 2.6, both the best fit and the data points themselves can be accommodated in the two scalar scenario.

3.1 The Problem with a Single Scalar BEC

While the NFW profile describes dark matter halo density to good precision at radii larger than \sim kpc, it is known that at sub-kpc distances the densities of typical galaxies approach constant values. Measurements of galaxy rotation curves yield the profile of the core density and core size across galaxies of different sizes [24, 64, 67, 68]. One can parametrize the density by

$$\rho(r) = \frac{\rho_c}{1 + r^2/R_c^2}, \quad (3.1)$$

where R_c is the radius where the density drops to half of the central density. By comparing with the measurement in [64], one can see the core size and core density can be fitted by $\rho_c \propto 1/R_c^\beta$, with $\beta \approx 1.3$ [24]. On the other hand, in a single scalar system, the scaling behavior is completely fixed by the scalar potential and dynamics can not change the mass-radius relation. For example, in the linear regime, it is H_{kin} balancing with H_{grav} , which gives the scaling shown in Eq. (2.20). This translates to $\rho \sim 1/R^4$. Similarly, one can try different polynomial potentials, and they result in different β 's, but none of them falls into $1 \lesssim \beta \lesssim 1.3$ even if one takes into account the scattering of the data. The values of the scaling index β are summarized in Table 1. This poses a challenge to using ultralight dark matter to address the core-cusp problem [24], which was one of the main motivations of ultralight dark matter [14, 69]. As we have briefly discussed, this problem can be

	H_{kin}	ϕ^4	ϕ^6
H_{grav}	$\beta = 4$	$\beta = \infty$	$\beta = -2$
$-\phi^4$	$(\beta = 2)$	n/a	$\beta = 0$

Table 1: The scaling index β for one scalar BEC with different scalar potentials. In any given regime, the system is balanced by two dominating terms, one in the top row and one from the left column. Note that $-\phi^4$ balancing H_{kin} is not stable.

understood as follows. When the system is composed of one scalar, the Hamiltonian can be written as

$$H \approx \frac{N_1}{2m_1 R_1^2} + \frac{\lambda_1 N_1^2}{32\pi f^2 R_1^3} - \frac{5Gm_1^2 N_1^2}{16R_1} - \frac{5GN_1^2}{16R_1^3}, \quad (3.2)$$

which leads to a fixed $M(R)$ relation. There is no room for the scalar dynamics to alter this relation, as both mass and radius are parametrized by the $\phi(0)$.

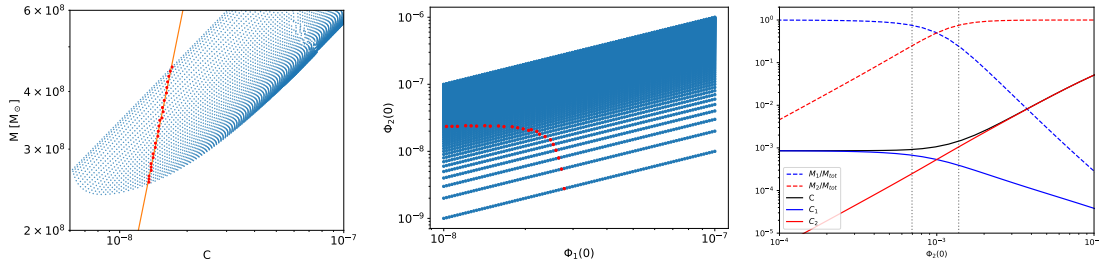


Figure 4: Left and middle: this is one example numerical scan over $\Phi_1(0)$, $\Phi_2(0)$ (blue points). Each blue point in the middle plot gives a unique mass profile, *i.e.* a blue point in the left panel in the $C - M$ space. The orange line is the best fit taken from [24]. From the numerical data cloud we pick the points to reconstruct the orange curve. These are shown as the red points in both panels. This particular scan is conducted with $m_1 = 10^{-22}$ eV, $m_2 = 2 \times 10^{-22}$ eV, and $\lambda_1 = \lambda_2 = \lambda_{12} = 0$. We scan $\Phi_1(0)$ and $\Phi_2(0)$ to show the existence of stable solutions. Right: we show the transition region from Φ_1 dominating to Φ_2 dominating by taking one slice of the scan with fixed $\Phi_1(0)$. One can see that indeed when one component mass is more than 75% the total mass, the compactness of the system is mostly determined by this mass component. We define the region between the grey dotted region to be the transition region.

3.2 Two-Scalar BEC to the Rescue

In this section, we first allow $\Phi_1(0)$ and $\Phi_2(0)$ to vary freely, and show that, while maintaining radial stability, there is parameter space that can accommodate the galactic data. We then comment on the implication for the dynamics of the two scalars.

We note that in the case of a two scalar system with $m_1 \neq m_2$, the curve in the $C - M$ plane is a smooth interpolation of the mass profile of each scalar as shown in Fig. 2. Scanning over the $\Phi_1(0) - \Phi_2(0)$ space gives us a region in the $C - M$ plane, with one-to-one correspondence of each $(\Phi_1(0), \Phi_2(0))$ point to a (C, M) point. On the other hand, galactic data points can be fit with a curve of $M \sim C^{2.4}$, *i.e.* $\rho \sim 1/R^{1.3}$. Therefore, by looking at the $(\Phi_1(0), \Phi_2(0))$ to (C, M) correspondence, one can find the one-dimensional curve that reproduces the best fit of the data. We show this explicitly in Fig. 4. We observe that a curve in $\Phi_1(0), \Phi_2(0)$ space can accommodate the best fit. In particular, we observe the mass profile of the total BEC is mostly dominated by one component if the component weighs more than 75% percent of the total mass. This indeed is a useful criteria in determining the dominant BEC component, as starting from this point the compactness is mainly determined by the dominant species. We show this in the right plot of Fig. 4.

As we discussed in Section 3.1, with two scalars one can accommodate the galactic data points even after taking into account the scattering of the data set, instead of just the $\rho \sim 1/R^{1.3}$ curve that best fits the data points. This can be done with the following procedure: we overlay the galactic data points with the numerical scan in the $C - M$ space (or equivalently in the $\rho - R$ space.) Then for each data point we can find a numerical point that is identical up to the scan resolution. We can then go back to the $\Phi_1(0), \Phi_2(0)$ space and identify the value for the $\Phi_1(0), \Phi_2(0)$ pair needed to reproduce this data point. The result is shown in Fig. 5.

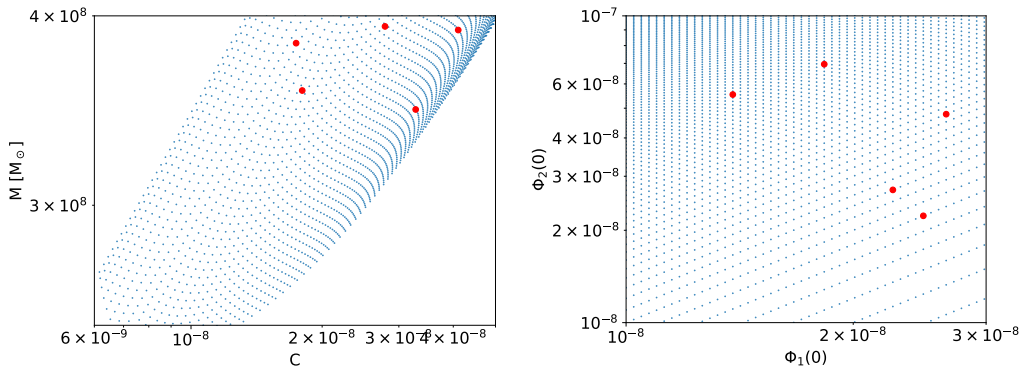


Figure 5: We show the numerical scan (blue) in both $C - M$ space (left) and $\Phi_1(0), \Phi_2(0)$ space (right). The red points are a few data points taken from [64]. This particular scan is conducted with $m_1 = 10^{-22}$ eV, $m_2 = 2 \times 10^{-22}$ eV, and $\lambda_1 = \lambda_2 = \lambda_{12} = 0$. See the main text for more details. We scan $\Phi_1(0)$ and $\Phi_2(0)$ to show solutions exist while the system maintains radial stability.

We emphasize that, however, this does not mean the two scalar BEC can accommodate any galactic data, or lacks predictability. While our approach only considers radial stability and existence of solutions of the BEC system, this exercise translates the galactic data to a requirement of the field value in the classical field configuration space. This requirement, shown in the right panels of Figs. (4-5), can be further constrained after the two scalar dynamics is taken into account. In addition, because of the extra scalar, there could be new constraints specific to the two scalar system, such as that related to the relaxation time scale. Since in this work we focus on the radial stability of the BEC system, we leave the study dedicated for constraining the two scalar BEC with galactic data for the future.

Lastly, we can extrapolate the numerical scan to the scenario where two scalars have a larger mass ratio. Given that we know the BEC system behaves like a single scalar when $\Phi_1(0) \gg \Phi_2(0)$ or vice versa, we can estimate how big a mass ratio is needed to accommodate all the data points. The extrapolation result is shown in Fig. 6 with $m_1 = 2 \times 10^{-24}$ eV and $m_2 = 2 \times 10^{-21}$ eV. This can be further used to constrain the two scalar model. At its face value, it seems that Lyman-alpha [70, 71] and subhalo mass function[22] might heavily constrain the lighter of the two scalar. However, it is known that the nonlinear interaction terms could play an important role in the evolution of cosmic perturbation and structure formation [4, 12, 72]. The extrapolation shown in Fig. 6 is in $m_1/m_2 \sim \mathcal{O}(10^{-3})$. If one fixes the radius, the BEC ratio M_1/M_2 needs to change three orders of magnitudes to go from ϕ_1 dominating the system to ϕ_2 dominating the system. More specifically, one needs that at $R_c \sim 10$ kpc, scalar one dominates, and at $R_c \sim 0.5$ kpc scalar two dominates.

To summarize, we stress two points that distinguish two scalar BEC from the single scalar BEC at the galactic scale: 1) With a single scalar, the mass and radius of the BEC is fixed by the scalar potential instead of scalar dynamics. As a result, it is highly nontrivial to find a potential that reproduces $\beta \approx 1.3$. This is verified by checking different combinations of potentials. This is no longer the case with two scalar BEC as we have a two-dimensional parameter space. In this case, both the scalar potential and the ratio of the two components (hence scalar dynamics) affect

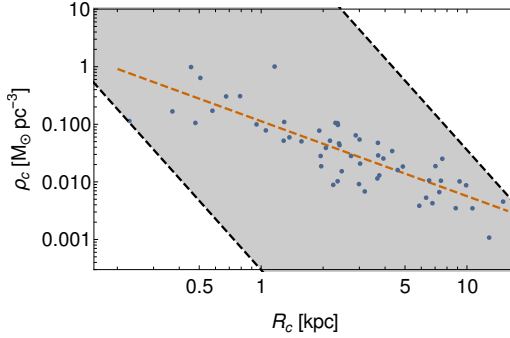


Figure 6: We extrapolate the numerical results to a larger mass separation, $m_1 = 2 \times 10^{-24}$ eV and $m_2 = 2 \times 10^{-21}$ eV. The grey region is what the two scalar BEC system covers with varying central density determined by $\Phi_1(0)$, $\Phi_2(0)$. One can see that it not only contains the best fit curve (orange) that represents $\rho_c \approx 1/R_c^{1.3}$, it also incorporates the scattering of the data. The data points are from [64], and fit adopted from [24]. We extrapolate the scalar mass gap m_1/m_2 , while use a range in the BEC fraction, M_1/M_2 , comparable to our numerical computations with smaller m_1/m_2 to show the existence of stable solutions.

the BEC’s mass-radius relation. 2) In the single scalar BEC, it is even harder to accommodate the scattering of the points, even if one manages to find a potential that reproduces $\rho \sim 1/R^{1.3}$, other than attributing it to observational errors. In the two scalar scenario, it is natural to have a scattering due to dynamics that leads to a fluctuation of $\Phi_1(0)/\Phi_2(0)$ from the best fit curve.

4 Stellar Scale BEC Structure

Having discussed galactic scale BEC, we now turn to the properties of two-scalar stellar scale BECs.

Whether it is possible to stabilize a BEC system determines how dense the system can become before it is destroyed by self-gravity. In the single scalar scenario, there is only one way to support gravity to form $C \sim \mathcal{O}(0.1)$ dense objects: by using repulsive $+\phi^{2n}$ potentials, whose model realizations have been shown to be non-trivial but possible [12]. Because of the presence of a second scalar, and non-gravitational interactions for both scalars and between them, we show that there are two new ways to support such systems to become dense enough. This could be relevant for gravitational wave signals from their binary mergers at LIGO-Virgo and LISA.

4.1 Non-gravitational Interaction between Two Scalars

In Section 2.6, we have already seen that the BEC structure can be drastically affected by the interaction $+\phi_1^2\phi_2^2$ term. This has significance for exotic compact searches at stellar scale, such as binary mergers at LIGO and LISA. In this section, we show more details on the effect of non-gravitational interactions in the nonlinear regime, with different combinations of λ_1 , λ_2 , λ_{12} . Among them, the most interesting case is $\lambda_1 < 0$, $\lambda_2 < 0$, $\lambda_{12} > 0$. Without the non-gravitational interaction proportional to λ_{12} , neither ϕ_1 or ϕ_2 can form a BEC system that is compact enough to be detectable say at LIGO through gravitational wave radiated by the binary mergers. However, $+\phi_1^2\phi_2^2$ pro-

vides pressure to support the gravitational collapse such that the system can be much denser as demonstrated in Fig. 7. This is consistent with the analysis in Eq. (2.22).

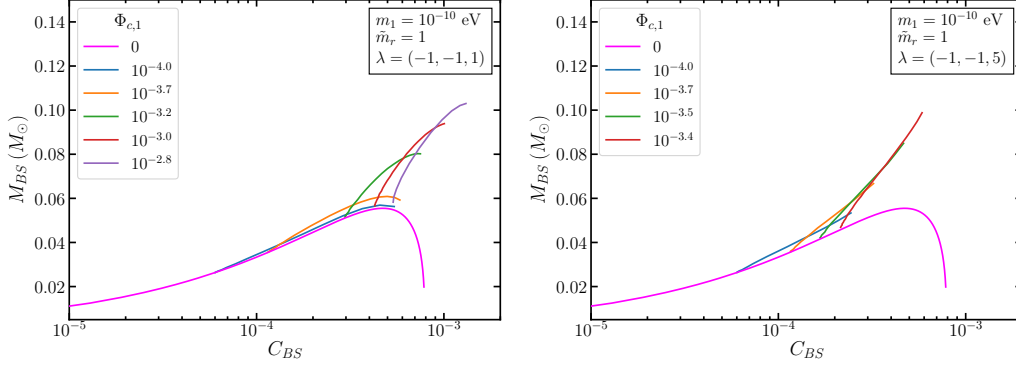


Figure 7: The mass vs compactness for a scan over $\Phi_2(0)$ for various fixed $\Phi_1(0)$. $\tilde{\lambda}_{12} = 1$ (left) is the same as right panel of Fig. 3, for comparison with $\tilde{\lambda}_{12} = 5$ (right). The magenta curve corresponds to the single scalar limit. All curves are generated by scanning over $\Phi_2(0)$. Different colors correspond to fixing $\Phi_1(0)$ to different values.

In the case of $-\phi_1^2\phi_2^2$, we note that just as the non-gravitational self-interaction counterpart $-\phi^4$, it renders the system unstable once this term becomes important. This can also be understood using Eq. (2.22). The effect is observed in the numerical solutions shown in Fig. 8.

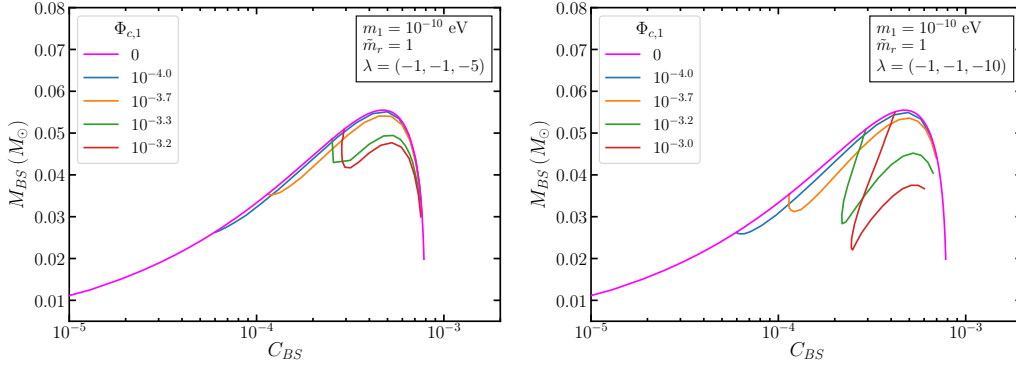


Figure 8: When $\tilde{\lambda}_{12} = -5$ (left) and $\tilde{\lambda}_{12} = -10$ (right). One can see the extra interaction term can dominate over the kinetic term earlier. Once it happens, the Hamiltonian loses its local minimum and the system becomes unstable. All curves are generated by scanning over $\Phi_2(0)$. Different colors correspond to fixing $\Phi_1(0)$ to different values.

We now comment on the difference between $\phi_1^2\phi_2^2$ and ϕ^4 types of interactions, and their impact on the resulted boson stars. One might think that if $\phi_1 \propto \phi_2$ everywhere, this two types of interactions are quite similar. However, this is rarely the case. At stellar scale, the formation history of BEC is highly nontrivial. In lack of a simulation, there is no reason to believe ϕ_1, ϕ_2 populate in every place proportionally. In the case of $V \sim -\phi_1^4 - \phi_2^4 + \phi_1^2\phi_2^2$, for example, there could exist boson stars consisting mainly ϕ_1 and those consisting mostly ϕ_2 due to their separate fragmentation

history [57]. Neither of the two types would be detectable because of the $-\phi^4$ potential. However, when the two stars merge, the interaction between the species now can support the self-gravity and allow the star to acquire more material to become denser, up to a point that it is detectable at LIGO/Virgo. In the case of $V \sim +\phi_1^4 + \phi_2^4 - \phi_1^2\phi_2^2$, on the other hand, the stars consisting mostly ϕ_1 or ϕ_2 could be very dense. However, unlike the single scalar BEC, the maximal compactness of either type is not capped by the metric fluctuation, but the term $-\phi_1^2\phi_2^2$. When two boson stars of kinds merge, it is more likely to result in an unstable BEC due to the $-\phi_1^2\phi_2^2$ term. In this case, one would not expect there remains a final boson star, but instead a phenomena dubbed Bosenova [4] could happen. Even before the two finishes merging, the resulted BEC system goes beyond the critical maximal mass, due to $-\phi_1^2\phi_2^2$. This could lead to gravitational wave different from those from single scalar ϕ^4 BEC mergers [40, 46]. As described in [57], attractive self-interaction leads to fragmentation, it is only natural to expect an attractive interaction between the two scalars could also lead to fragmentation, but only when BEC's of different types encounter. This could lead to novel nonlinear behaviors in boson star formations. In both scenarios above, we see the difference between $\phi_1^2\phi_2^2$ and ϕ^4 boson stars related to their formation history.

On the aspect of observation, $\phi_1^2\phi_2^2$ boson stars are also quite distinct from ϕ^4 boson stars. From Eq. (2.22), one can see that when ϕ_2^4 term balances self-gravity, it leads to the usual mass curve, $M \propto C$. However, when $\phi_2^2\phi_1^2$ balances self-gravity with ϕ_1 being a sub-component, the mass curve is

$$M \propto M_1^{1/3} C^{2/3}. \quad (4.1)$$

When the sub-component M_1 is fixed, the mass curve is different from a $+\phi^4$ BEC system. On the other hand, due to the non-linear effect of gravity at small scales, one naturally expect the ϕ_1 component, M_1 to vary from star to star. As a result, we expect some scattering around this mass curve, which is another feature that ϕ^4 mass curve does not have.

On the aspect of model building, as we will show in the following sections, ultralight scalars with interaction between multiple species can be achieved naturally. It is shown in [12] that it is nontrivial to build a $+\phi^4$ theory. Given that axions/ALPs all have a $-\phi^4$ interaction, we show that they can indeed lead to compact BEC structures if there are extra interactions - such as $+\phi_1^2\phi_2^2$ - that arises naturally from collective symmetry breaking and stabilizes the system, it could lead to dense axion stars. This hints for a different class of models compared to those that lead to a $+\phi^4$ theory.

4.2 Implication for Gravitational Wave Detection

In the past, LIGO-Virgo have observed numerous binary black hole mergers and a few neutron star mergers. Besides the tests of GR, there have been studies on probing new physics by detecting binary mergers consisting of exotic compact objects [26, 40, 51, 53, 73] to name a few. While axions are well studied and motivated in particle physics, the compactness of axion stars is far below LIGO sensitivity, which renders a direct detection of axion star binary mergers impossible⁴. This changes when one takes into account extra scalars with non-gravitational interactions between

⁴It is noted that [74] argues that there exist a dense branch for axion stars, yet [32] shows the lifetime of the dense branch is too short.

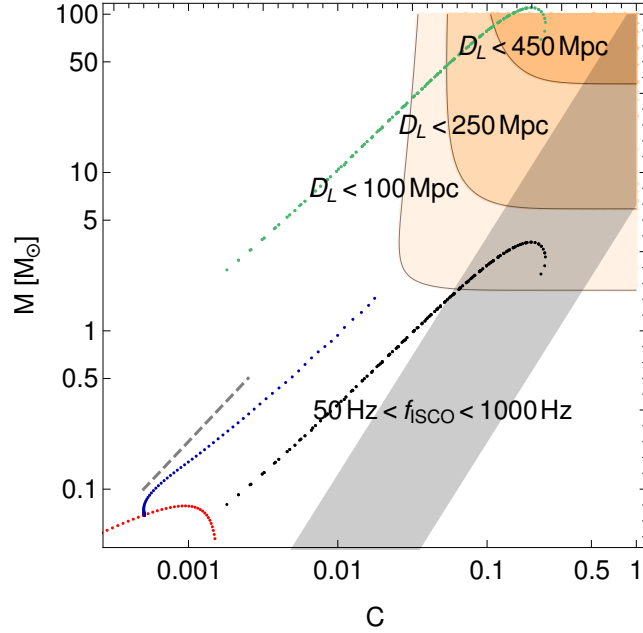


Figure 9: The orange bands correspond to the required $C - M$ region that can give SNR $\rho > 8$ needed for detection, given different luminosity distances. The grey band corresponds to the region that f_{ISCO} is in the LIGO sensitivity band, 50 Hz \sim 1000 Hz. The red curve is the mass-compactness profile of a single axion with attractive ϕ_1^4 with $\lambda_1 = -0.5$. The blue curve is achieved by adding a second axion to the red curve while fixing $\phi_1(0)$ and varying $\phi_2(0)$. The interactions are $\lambda_1 = \lambda_2 = -0.5, \lambda_{12} = +5$. We only show part of the curve due to computational complexity related to the stiffness in the equations. The black and green curves are achieved by varying both $\phi_1(0)$ and $\phi_2(0)$, with the same interactions as the blue curve. The red and blue have mass set to 10^{-10} eV, the black 3×10^{-10} eV, and green 10^{-11} eV. The grey dashed line is a guide for the eye, to show $M \propto C$, the mass relation one expects from a single scalar $+\phi^4$ BEC. One can see that indeed, when $\phi_1(0)$ is fixed, the mass curve has a slope smaller than one, as discussed in Eq. (18).

them. As we have shown in Section 4.1, a repulsive $+\phi_1^2\phi_2^2$ can support the system made of two axions up to $\mathcal{O}(0.2)$ compactness, a behavior that was only known to exist in repulsive self-interaction system [40].

For a generic binary system, the gravitational wave during its inspiral phase is

$$f_{GW} = \sqrt{\frac{M_1 + M_2}{\pi^2 \ell^3}}, \quad (4.2)$$

where M_1, M_2 are the masses of each inspiral object, ℓ the major semi-axis. Assuming equal mass system, the innermost stable circular orbit (ISCO) happens at $\ell = 6R$, with R being the radius of

the star. The gravitational wave frequency at ISCO can be expressed as

$$f_{ISCO} = \sqrt{\frac{2M}{\pi^2(6R)^3}} = \frac{C^{3/2}M_{Pl}^2}{2\pi \cdot 3^{3/2}M} \approx 50 \text{ Hz} \left(\frac{M_\odot}{M}\right) \left(\frac{C}{0.04}\right)^{3/2}. \quad (4.3)$$

From the ISCO frequency one can extract the size of each object. The signal strength in frequency space is given as [75]

$$\begin{aligned} \tilde{h}(f) &= \left(\frac{\sqrt{5/24}G_N^{5/6}}{\pi^{2/3}c^{3/2}}\right) \frac{M_c^{5/6}}{f_{GW}^{7/6}D_L} \\ &\stackrel{ISCO}{\approx} 7.2 \times 10^{-24} \text{ Hz}^{-1} \left(\frac{M}{M_\odot}\right)^2 \left(\frac{C}{0.04}\right)^{-7/4} \left(\frac{D_L}{100 \text{ Mpc}}\right)^{-1}, \end{aligned} \quad (4.4)$$

where the second line is estimated at $f_{GW} = f_{ISCO}$. The signal-to-noise ratio (SNR) is computed as

$$\rho^2 = 4 \int_0^{f_{ISCO}} \frac{|\tilde{h}(f)|^2}{S_n(f)} df, \quad (4.5)$$

where $S_n(f)$ is the detector noise power spectral density [76]. We require $\rho > 8$ for a possible detection. The LIGO sensitivity band is shown in Fig. 9, together with the mass-compactness profile of the BEC objects. It is observed that with a single axion-like particle ($-\phi^4$ self-interaction) the BEC structure is far from LIGO sensitivity band, while a repulsive interaction between the two scalars supports the system to $\mathcal{O}(0.2)$ region that is relevant at LIGO.

With gravitational wave detectors LIGO-Virgo finishing O3 and being upgraded for higher sensitivity, KAGRA [77] started the observation run, and LIGO-India planned to join the network in the near future, we emphasize that this serves as an example that the interferometry facilities have potential to probe fundamental particles and interesting interactions beyond gravity.

Intriguingly, LIGO-Virgo have recently detected a compact binary merger event (GW190521) with a total mass of $150 M_\odot$ [78, 79], with the primary mass $85_{-14}^{+21} M_\odot$ falling in the mass gap predicted by pair-instability supernova theory, $65 - 120 M_\odot$. In Fig. 9, we show that a BEC system made of two scalars of mass $\sim 10^{-11}$ eV can produce compact structures in the range of $100 M_\odot$. While a dedicated analysis is needed to investigate its GW signals in our model, it is shown that certain types of boson stars could potentially reproduce the event [80].

4.3 Comparison with previous work

Before we move on to the particle model, we briefly discuss the relation and differences with previous studies on multiple species BEC [59] and [58]. In [59] the scenario of multiple axions are discussed in details. We list the main differences between this work and [59] and comment on them in more details.

- the analysis of [59] is performed in the non-relativistic limit, while we solve the full EKG system;
- between different species [59] assume they only interact gravitationally, while we allow interactions $\propto |\phi_1|^2|\phi_2|^2$;

- analytical approximation to the solution of Schödinger-Newton equation is carefully studied by [59] while we solve the EKG system both numerically and analytically.

We note that the first two points are relevant when the field value is large. In particular, the first point captures the GR effect so that it allows us to apply the method to both the galactic scale BEC and the stellar scale. We also observe that in Eq. (2.19) our Hamiltonian precisely reproduces the result of [59] (Eq. 2.15 therein) in the limit $R_1 \approx R_2$. When $R_1 \neq R_2$, we have $\mathcal{O}(1)$ difference due to the choice of our anzats. We stress that we contain higher order terms $H_{metric} \propto G/R^3$, which have the origin of metric perturbation beyond Newtonian gravity, hence only shows up when one solves the EKG system. This is discussed in [40] with a single species.

Astrophysical implications of multiple axions are discussed in [58]. We note a few differences compared to this work.

- The work of [58] uses the so-called independent approximation, which treats solitons of different sizes separately. This allows them to go in to a regime where the mass of the heaviest one is four orders of magnitude larger than the lightest one.
- Similar to [59], [58] uses the Newtonian limit.
- [58] assumes the scalars only interact gravitationally.
- The observational data include the Fornax Galaxy, central Milky Way; Ultra Faint Galaxies; and globular cluster 47 Tuc. In this work our fit at galaxy scale is motivated by [64].
- [58] also performs a Bayesian analysis to fit with the scalar mass, with the presence of extra nuisance parameters from the astrophysical environment.

5 Model Realization

In this section we discuss how multiple light scalars with repulsive interactions between them can be realized from the point of view of particle physics model building. It is well known that light scalars can be generated by identifying them as pseudo-Nambu-Goldstone bosons (pNGB) after the spontaneous breaking of some approximate global symmetry. Applications of this idea related to addressing the electroweak hierarchy include leveraging breaking patterns such as $SU(5) \rightarrow SO(5)$ [81], $SU(3) \times SU(3) \rightarrow SU(3)$ [82], $SU(6) \rightarrow Sp(6)$ [66], and $SO(6) \rightarrow SO(5)$ [83], to name a few. It was shown in [12] that similar collective symmetry breaking mechanisms can be used to generate repulsive self-interaction in the context of ultra-light dark matter, and potentially a large separation between the scalar mass and the symmetry breaking scale, which is needed to ensure the interaction between the scalars remains weak. We show that this can be extended to the two scalar scenario, which leads to a repulsive interaction between the two light scalars while being technically natural.

After spontaneous symmetry breaking of a global symmetry, such as $SU(6)$ to $Sp(6)$ in [66], one could end up with the following effective potential

$$c_1 f^2 \left| s + \frac{i}{2f} [\phi_2^\dagger \phi_1] \right|^2 + c_2 f^2 \left| s - \frac{i}{2f} [\phi_2^\dagger \phi_1] \right|^2, \quad (5.1)$$

where s, ϕ_1, ϕ_2 are pNGB living in the quotient group, $SU(6)/Sp(6)$ in this example, and $c_{1,2}$ dimensionless coefficients that can be naturally small yet positive. s is a singlet under gauge transformations, while both ϕ_1 and ϕ_2 are gauge multiplets, doublets of two $SU(2)$'s in the specific case. $[\phi\phi]$ indicates a proper contraction with the gauge indices. One can see that each of the two terms in Eq. (5.1) preserves a direction of the infinitesimal global transformation:

$$\begin{aligned}\phi_1 &\rightarrow \phi_1 + \epsilon_1, \\ \phi_2 &\rightarrow \phi_2 + \epsilon_2, \\ s &\rightarrow s - \frac{i}{2f}([\epsilon_2^\dagger \phi_1] + [\phi_2^\dagger \epsilon_1])\end{aligned}\tag{5.2}$$

for the first term, and

$$\begin{aligned}\phi_1 &\rightarrow \phi_1 + \epsilon_1, \\ \phi_2 &\rightarrow \phi_2 + \epsilon_2, \\ s &\rightarrow s + \frac{i}{2f}([\epsilon_2^\dagger \phi_1] + [\phi_2^\dagger \epsilon_1])\end{aligned}\tag{5.3}$$

for the second term. Equation (5.1) generates a mass for the singlet s to be $m_s^2 \sim f^2(c_1 + c_2)$. Integrating out the scalar s , we have a interaction between ϕ_1 and ϕ_2 at tree level

$$V_{int}(\phi_1, \phi_2) \sim \frac{c_1 c_2}{c_1 + c_2} |[\phi_2^\dagger \phi_1]|^2.\tag{5.4}$$

Mass terms for ϕ_1 and ϕ_2 are generated at one loop level,

$$V_m(\phi_1, \phi_2) \sim m_1^2 |\phi_1|^2 + m_2^2 |\phi_2|^2 + m_{12}^2 ([\phi_1^\dagger \phi_2] + h.c.),\tag{5.5}$$

where

$$m_1^2 \sim m_2^2 \sim \frac{c_1 c_2}{16\pi^2} f^2,\tag{5.6}$$

where we neglect the logarithmic part that is $\sim \mathcal{O}(1)$. Choosing a small $c_{1,2}$ leads to a large separation between the symmetry breaking scale and the scalar mass. The low energy potential is $V = V_m + V_{int}$. When $m_{12} \rightarrow 0$, the system has a total of four complex scalars that enjoy two separate $U(1)$'s, with generator θ_1 and θ_2 :

$$\begin{aligned}\phi_1 &\rightarrow e^{+i\theta_1} \phi_1, \\ \phi_2 &\rightarrow e^{+i\theta_2} \phi_2.\end{aligned}\tag{5.7}$$

We hasten to add that the model we have proposed, which falls under the genre of ‘‘Little Dark Matter’’ models introduced in [12], is a proof-of-principle model construct of two-scalar ultralight scalar system with a repulsive interaction.

6 Conclusion

In this paper, we have demonstrated interesting features in a two scalar BEC system with spherical symmetry. We have developed numerical code to solve the system exactly. We first verified its

stability against radial perturbations by performing numerical time evolution. We then went on to show two main features of the system:

1) **Galactic Scale:** The difference of the mass of the two scalars allows us to extend the BEC mass profile in the $C - M$ plane from a curve to a region, hence open up new parameter space. This is due to the fact that, with a fixed set of theory parameters, $[M_{BS}(\Phi_1(0)), C_{BS}(\Phi_1(0))]$ is extended to $[M_{BS}(\Phi_1(0), \Phi_2(0)), C_{BS}(\Phi_1(0), \Phi_2(0))]$. We show that this has interesting indications to the problem [24] that one scalar BEC cannot fit the dark matter core profile at the galactic scale.

2) **Stellar Scale:** At the stellar scale with $m \sim 10^{-10}$ eV, we show that the non-gravitational interactions between the two scalars $\Phi_1^2 \Phi_2^2$ can play an important role in stabilizing the system up to high compactness. This is similar to the fact that $+\phi^4$ self-interaction stabilizes the system and achieves compactness $C \sim \mathcal{O}(0.2)$. This has important implications for possible detections at LIGO-Virgo. In addition, with $m_1 \neq m_2$, we show that the transitioning from Φ_1 dominating to Φ_2 dominating holds for different choices of λ 's. In particular, in the case of $\lambda_1 \cdot \lambda_2 < 0$, the stability is determined by the dominating scalar with highest occupation number. This also hints at interesting phenomenology at gravitational detectors such as LIGO-Virgo and LISA.

Based on our results, there are several interesting future directions. For example: how does the presence of extra scalar(s) affect the cosmological evolution compared to the single scalar scenario? Given that it is known non-gravitational self-interaction can lead to an altered structure formation history as demonstrated in [12, 72], the non-gravitational interaction between the two scalars will likely also change the structure formation process. This might change the bounds on ultra-light dark matter bounds derived from Lyman-alpha [70, 71] and subhalo mass function [22].

In addition, with two scalars the BEC spans a region in the mass-compactness plane instead of forming a curve. One could ask if all points in that region are equally possible to form. The answer is likely negative as galactic scale dynamics might affect the relation among the central density of each scalar. However, addressing this issue is beyond the scope of this work, where our focus is on the mass profile of stable BEC systems. Indeed, the two questions described above may be related, and addressing them requires dedicated simulations. We leave this for future work.

Acknowledgments

We would like to thank Kfir Blum, Joshua Eby, JiJi Fan, Michael Geller, Mark Hertzberg, Hitoshi Murayama, Tim Tait, and Tomer Volansky for useful discussions at different stages of the work. We would also like to thank the two anonymous referees for their useful comments, which contribute to the improvement of the work. HG and KS are supported by DOE Grant desc0009956. CS is supported by the Foreign Postdoctoral Fellowship Program of the Israel Academy of Sciences and Humanities, partly by the European Research Council (ERC) under the EU Horizon 2020 Programme (ERC-CoG-2015 - Proposal n. 682676 LDMThExp), and partly by Israel Science Foundation (Grant No. 1302/19). JS acknowledges the REU program at the University of Oklahoma, which is supported by NSF grant 1659501.

A Einstein Tensor

We start with the metric as follows,

$$g_{\mu\nu} = \begin{bmatrix} -B(r) & 0 & 0 & 0 \\ 0 & A(r) & 0 & 0 \\ 0 & 0 & r^2 & 0 \\ 0 & 0 & 0 & r^2 \sin^2 \theta \end{bmatrix}. \quad (\text{A.1})$$

We can then write out the non-zero Christoffel symbol components as

$$\begin{aligned} \Gamma_{tr}^t &= \frac{B'(r)}{2B(r)}, & \Gamma_{tt}^r &= \frac{B'(r)}{2A(r)}, \\ \Gamma_{rr}^r &= \frac{A'(r)}{2A(r)}, & \Gamma_{\theta\theta}^r &= -\frac{r}{A(r)}, & \Gamma_{\phi\phi}^r &= -\frac{r \sin^2(\theta)}{A(r)}, \\ \Gamma_{r\theta}^\theta &= \frac{1}{r}, & \Gamma_{\phi\phi}^\theta &= -\cos(\theta) \sin(\theta), \\ \Gamma_{r\phi}^\phi &= \frac{1}{r}, & \Gamma_{\theta\phi}^\phi &= \cot(\theta), \end{aligned} \quad (\text{A.2})$$

from which the Einstein tensor G_μ^ν can be calculated

$$\begin{aligned} G_t^t &= -\frac{A'(r)}{rA(r)^2} + \frac{1}{r^2A(r)} - \frac{1}{r^2}, \\ G_r^r &= \frac{B'(r)}{rA(r)B(r)} + \frac{1}{r^2A(r)} - \frac{1}{r^2}, \\ G_\theta^\theta &= -\frac{A'(r)B'(r)}{4A(r)^2B(r)} - \frac{A'(r)}{2rA(r)^2} + \frac{B''(r)}{2A(r)B(r)} - \frac{B'(r)^2}{4A(r)B(r)^2} + \frac{B'(r)}{2rA(r)B(r)}, \\ G_\phi^\phi &= -\frac{A'(r)B'(r)}{4A(r)^2B(r)} - \frac{A'(r)}{2rA(r)^2} + \frac{B''(r)}{2A(r)B(r)} - \frac{B'(r)^2}{4A(r)B(r)^2} + \frac{B'(r)}{2rA(r)B(r)}. \end{aligned} \quad (\text{A.3})$$

B Numerical Procedure

Typically the equations of motion are solved using the shooting method which is successful in the one scalar case where the solution can easily converge to the ground state configuration. The equations get numerically difficult to solve when extra scalars are introduced, particularly in the nonlinear regime where λ can have significant contribution to the total mass. A workaround was found by implementing a relaxation algorithm into our personal code which proved successful in solving the differential equations.

B.1 Relaxation Method

To find numerical solutions, we use the relaxation algorithm described in chapter 18 of *Numerical Recipes* [65]. We first write the system in the standard form

$$\mathbf{y}'(t) = \mathbf{g}(t, \mathbf{y}). \quad (\text{B.1})$$

. We want to solve this system over the interval $[a, b]$. We start with a trial solution $\bar{\mathbf{y}}$ that satisfies all boundary conditions. Then we choose a set of evenly spaced points $\{t_k\}_{k=0}^{M-1}$ spanning the interval. At each point except for t_0 , we form the difference equations

$$\mathbf{E}_k = \bar{\mathbf{y}}(t_k) - \bar{\mathbf{y}}(t_{k-1}) - (t_k - t_{k-1})\mathbf{g}(t_{\text{av}}, \bar{\mathbf{y}}_{\text{av}}), \quad (\text{B.2})$$

where t_{av} and $\bar{\mathbf{y}}_{\text{av}}$ are the averages of t_k and t_{k-1} , and $\bar{\mathbf{y}}(t_k)$ and $\bar{\mathbf{y}}(t_{k-1})$ respectively. We want to adjust our trial solution so that each \mathbf{E}_k vanishes. Let $\Delta\bar{\mathbf{y}}(t)$ represent the adjustments we need to make to the trial solutions at each of the grid points so that

$$\mathbf{E}_k(\bar{\mathbf{y}}(t_{k-1}) + \Delta\bar{\mathbf{y}}(t_{k-1}), \bar{\mathbf{y}}(t_k) + \Delta\bar{\mathbf{y}}(t_k)) = 0. \quad (\text{B.3})$$

We can approximate $\Delta\bar{\mathbf{y}}(t)$ at each of the grid points by expanding \mathbf{E}_k as a first-order Taylor series in $\Delta\bar{\mathbf{y}}$. Then we have

$$\begin{aligned} \mathbf{0} &= \mathbf{E}_k(\bar{\mathbf{y}}(t_{k-1}) + \Delta\bar{\mathbf{y}}(t_{k-1}), \bar{\mathbf{y}}(t_k) + \Delta\bar{\mathbf{y}}(t_k)) \\ &\approx \mathbf{E}_k(\bar{\mathbf{y}}(t_{k-1}), \bar{\mathbf{y}}(t_k)) + \sum_{n=0}^{N-1} \frac{\partial \mathbf{E}_k}{\partial \bar{y}_n(t_{k-1})} \Delta\bar{y}_n(t_{k-1}) + \sum_{n=0}^{N-1} \frac{\partial \mathbf{E}_k}{\partial \bar{y}_n(t_k)} \Delta\bar{y}_n(t_k), \end{aligned} \quad (\text{B.4})$$

where N is the dimension of \mathbf{y} and $\bar{y}_n(t_k)$ is the n th component of $\bar{\mathbf{y}}(t_k)$. Since we already know $\mathbf{E}_k(\bar{\mathbf{y}}(t_{k-1}), \bar{\mathbf{y}}(t_k))$, this gives us $N \cdot (M - 1)$ equations for $N \cdot M$ unknowns. The remaining N equations come from the boundary conditions.

These equations, together with the boundary conditions, allow us to solve for the first-order corrections $\Delta\bar{\mathbf{y}}(t_k)$. By adding these corrections to $\bar{\mathbf{y}}(t)$, we obtain a new trial solution. We then iteratively repeat this process with the new trial solution until the trial solutions converge. We determine convergence by measuring the average size of the components of the correction vectors $\Delta\bar{\mathbf{y}}(t_k)$. Once the average size of the corrections becomes small enough, we assume that the trial solutions have converged to the correct solution.

B.2 Static Case

The profiles for $A, B, \Phi_1, \Phi_2, \Phi'_1,$ and Φ'_2 are found by solving the equations of motion using the relaxation method. The boundary conditions at the origin and at infinity are given by

$$\Phi_n(0) = \Phi_{c,n} \quad (\text{B.5})$$

$$\Phi'_n(0) = 0 \quad (\text{B.6})$$

$$A(0) = 0 \quad (\text{B.7})$$

$$B(0) = B_0 \quad (\text{B.8})$$

$$\lim_{r \rightarrow \infty} \Phi_n(r) = 0 \quad (\text{B.9})$$

$$\lim_{r \rightarrow \infty} \Phi'_n(r) = 0 \quad (\text{B.10})$$

$$\lim_{r \rightarrow \infty} B(r) = \frac{1}{A(r)}. \quad (\text{B.11})$$

For appropriate choices of the eigenvalues $\mu_{1,2}$ we can find the ground state configurations for $\Phi_{1,2}$. Although $\Phi_{1,2}$ must satisfy all of the boundaries conditions above, we can introduce constant

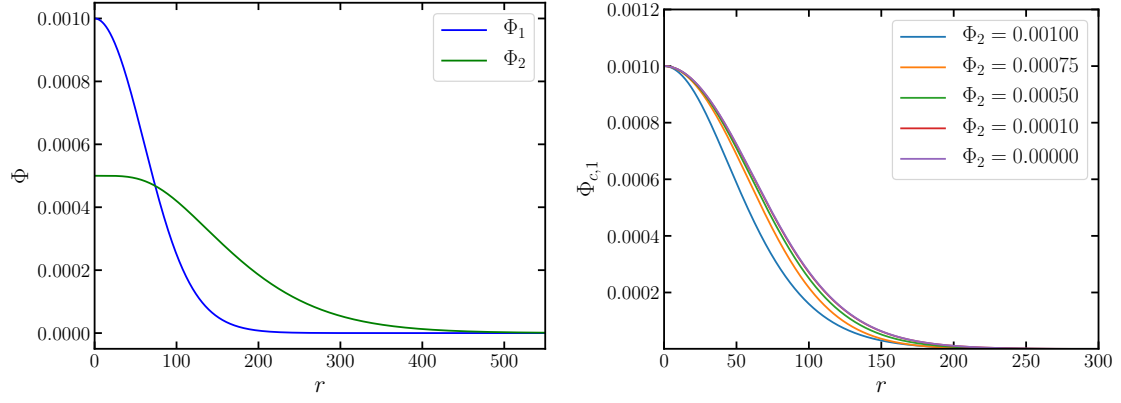


Figure 10: The left figure includes the wave forms for Φ_1 and Φ_2 . The right figure fixes $\Phi_1(0) = 0.001$ and shows the effect of changing $\Phi_2(0)$. For $\Phi_2(0) \ll \Phi_1(0)$ the profiles behave like the one scalar case with $\Phi_c = 0.001$. When $\Phi_1(0) < \Phi_{2,1}$ we see a difference compared to the single boson case. Calculations were performed with $\lambda_1 = \lambda_2 = \lambda_{12} = 1$, $m_1 = 10^{-10}$ GeV, and $\tilde{m}_r = 0.5$.

differential equations to the equation of motion for the parameters of the problem without changing the physics of the system. This allows us to exploit the iterative process of the relaxation method to guess the values for $\mu_{1,2}$ until they converge to correct values as $r \rightarrow \infty$. We do this by including the following differential equations for $\mu_{1,2}$ into the relaxation method

$$\frac{d\mu_n}{dr} = 0, n=1,2 \quad (\text{B.12})$$

which allows in total 6 differential equations and 13 boundary conditions to be met. The numerical procedure to solve the equations of motion is as follows:

1. Choose an initial guess for $A, B, \Phi_{1,2}, \Phi'_{1,2}$ that satisfies the boundary conditions.
2. Run relaxation method on an interval $[0, r_{\text{out}}]$
3. If the error begins to diverge, recursively try a smaller interval and use that as an initial guess until it finds a solution.
4. If $\Phi_{1,2} < 0$ or $\Phi'_{1,2} > 0$, try again on a smaller interval with more grid points because an excited state was found.
5. Check if $\Phi_{1,2}(r_{\text{out}}) < \epsilon$ where ϵ is a percentage of the initial central density. If true, $\Phi_{1,2}$ has decayed to its asymptotic value at $r_{\text{out}} = \infty$ and the ground state has been found.
6. If condition 5 is not met increase r_{out} and start from 2.

Once the ground state solutions are found for Φ_1 and Φ_2 , the initial value of B_0 and the eigenvalues, μ_1 and μ_2 will be found to guarantee the boundary values are met. A sample plot of $\Phi_{1,2}$ is included in Fig. 10. The left figure is a representative plot of the wave profiles for Φ_1 and Φ_2 . The equations of motion couple both scalars together. We can see from the right figure the impact

the second scalar has on Φ_1 by varying its central density. For $m_1 = 10^{-10}$ eV and $\tilde{m}_r = 0.5$, the equation of motions look like the single scalar case when $\Phi_2(0) \ll \Phi_1(0)$. However, when $\Phi_2(0) \sim \Phi_1(0)$, the wave profile of Φ_1 deviates from the single scalar case as expected.

B.3 Time Evolution

To ensure the stability of the equations of motion, we must first check how the equations of motion evolve under small radial perturbations. We first approximate the partial derivatives in the equations motion as central finite differences :

$$\frac{\partial f}{\partial r} = \frac{f_{j+1}^i(r, t) - f_{j-1}^i(r, t)}{2\Delta r}, \quad (\text{B.13})$$

$$\frac{\partial f}{\partial t} = \frac{f_j^{i+1}(r, t) - f_j^i(r, t)}{\Delta t}, \quad (\text{B.14})$$

$$\frac{\partial^2 f}{\partial r^2} = \frac{f_{j+1}^i(r, t) - 2f_j^i(r, t) + f_{j-1}^i(r, t)}{\Delta r^2}, \quad (\text{B.15})$$

$$\frac{\partial^2 f}{\partial t^2} = \frac{f_j^{i+1}(r, t) - 2f_j^i(r, t) + f_j^{i-1}(r, t)}{\Delta t^2}, \quad (\text{B.16})$$

where i and j correspond to steps in space and time respectively. The step sizes are given by Δr and Δt . We note that these expressions are only valid for $i \in [1, N_t - 1]$ and $j \in [1, N_r - 1]$ where $i = 0, \dots, N_t$ and $j = 0, \dots, N_r$. For the endpoints we use either backwards or forward difference. Using finite differences we see that the two Klein-Gordon equations of motion give

$$\Phi_{j,(1,2)}^{i+1} = 2\Phi_{j,(1,2)}^i - \Phi_{j,(1,2)}^{i-1} + \Delta t^2 F(r, A, B, \Phi_1, \Phi_2, A', B', \Phi_1', \Phi_2'). \quad (\text{B.17})$$

To find the time evolution of the system we perform the following steps:

1. Solve the static equations of motion.
2. Perturb $\Phi_{1,2}$ by a factor of $(1 + \epsilon)$.
3. Perform the first time step in the Klein-Gordon equations for $\Phi_{1,2}$ using Eq B.17 where the static solution is $\Phi_{j,(1,2)}^{i-1}$ and the perturbed solution is $\Phi_{j,(1,2)}^i$.
4. Perturb $\Phi_{1,2}$ by a factor of $(1 + \epsilon)$.
5. Solve the remaining two differential equations using the Relaxation Method to get A_j^{i+1} and B_j^{i+1} .
6. Repeat.

Sufficient time steps were performed following the above procedure to ensure the stability of the time evolution equations for sample benchmark points.

The physical time, t , used in the equations of motion is in units of m^{-1} with the corresponding dimensionless time, \tilde{t} , given by

$$t = \frac{1}{m} \tilde{t}. \quad (\text{B.18})$$

The time evolution of the single scalar case was previously studied in [29] for both the stable and unstable branch with different re-scaled quantities. To match with the notation there, we compare our dimensionless variable with the ones used in [29]. The potential used in the analysis considers the non-relativistic interaction term

$$V_{nr} = \frac{\psi^{*2}\psi^2}{16f^2} \quad (\text{B.19})$$

with the following ansatz for the scalar field

$$\Phi = \frac{1}{\sqrt{m}}\Psi(r) = \sqrt{\frac{N}{\pi m R^3}} e^{-r/R} \quad (\text{B.20})$$

where R is the decay length scale and N is the total number of particles. The re-scaled quantities are

$$\begin{aligned} R &= \frac{M_{Pl}}{mf} \hat{R} \\ N &= \frac{M_{Pl}f}{m^2} \hat{N} \\ \Psi &= \frac{\sqrt{m}f^2}{M_{Pl}} \hat{\Psi}, \end{aligned}$$

where \hat{X} is the dimensionless counterpart of variable X used in [29]. The corresponding time evolution equation of the scalar field in dimensionless units is

$$i \frac{\partial \hat{\Psi}}{\partial \hat{t}} = -\frac{1}{2\hat{r}} \frac{\partial^2}{\partial \hat{r}^2} (\hat{r} \hat{\Psi}) + \hat{\phi}_N \hat{\Psi} - \frac{1}{8} |\hat{\Psi}|^2 \hat{\Psi} \quad (\text{B.21})$$

where $\hat{\phi}_N$ is the newtonian potential. If we restore the physical parameters in the above equation, the physical time will become

$$t = \frac{M_{Pl}^2}{mf^2} \hat{t}. \quad (\text{B.22})$$

This allows for simple comparison by setting the physical times equal to each other. The scalar field is related by

$$\tilde{\Phi} = \frac{\sqrt{4\pi}f^2}{M_{Pl}^2} \hat{\Psi}. \quad (\text{B.23})$$

C Single Scalar Limit

In this section we verify that in the limit of $m_1 = m_2$, and $\lambda_1 \sim \lambda_2$, one recovers the single scalar limit as expected. In the non-relativistic section it was stated that the scalar limit occurs when one of the number densities dominates over the other. The number density in the non-relativistic limit is given by

$$N_i = 4\pi \int dr r^2 m_i |\Phi_i(r)|^2 \quad (\text{C.1})$$

where the index $i = 1, 2$ corresponds to each scalar, and the integral is over the scalars central density. This is related to the mass of the star for the two scalar system as

$$M = m_1 N_1 + m_2 N_2. \quad (\text{C.2})$$

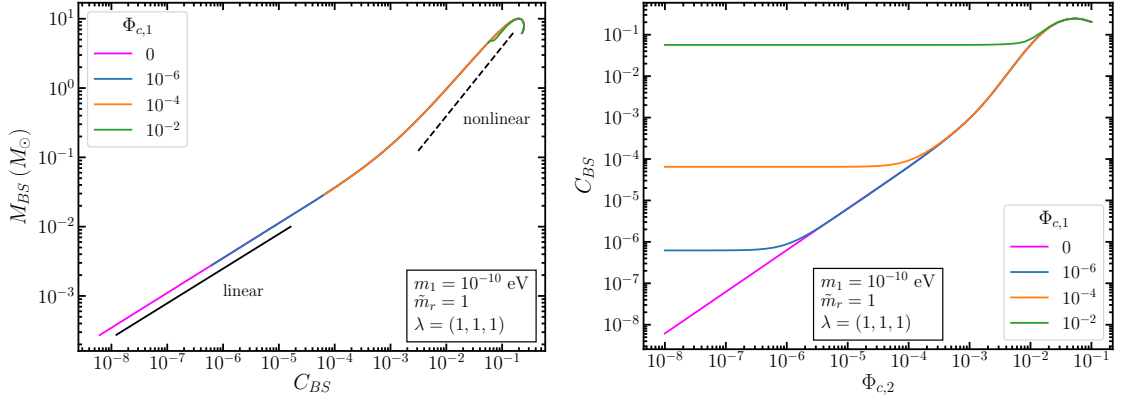


Figure 11: BEC structure obtained with equal mass for the two scalars and different fixed central density of one scalar, $\Phi_{1,c}$, and different coupling choices. Left: the total mass vs compactness for various $\Phi_1(0)$ and $\Phi_2(0)$ for $\lambda_1 = 1$, $\lambda_2 = 1$, and $\lambda_{12} = 1$. The solid lines correspond to fixed $\Phi_1(0)$ while scanning over $\Phi_2(0)$. The solid magenta curve corresponds to the single scalar limit by setting $\Phi_1(0) = 0$ and scanning over $\Phi_2(0)$. The solid and dashed black lines represent the linear and nonlinear scaling cases when M_{BS} is derived from Eq. 2.19. Right: the compactness versus $\Phi_2(0)$ for different values of $\Phi_1(0)$. It plateaus to a fixed value of C_{BS} when $\Phi_2(0)$ is small and the star is dominated by Φ_1 . The turning point occurs when $\Phi_2(0) \approx \Phi_1(0)$

The single scalar limit is taken for when $\Phi_2(0) \gg \Phi_1(0)$ and vice versa. In Fig. 11 we show that the single scalar limit can be recovered when $\Phi_1(0)$ is chosen to be small. In Fig. 12, we show C_2 versus M_2 for the second scalar's contribution to the BEC system mass and compactness where we scan over $\Phi_2(0)$ for different values of fixed $\Phi_1(0)$. The curves represent scans over the two central densities. Each curve for the two scalar scans begin with $\Phi_2(0) \ll \Phi_1(0)$ on the far left points. The curves all begin with masses much below the single scalar limit which means that the second scalar contribution to the total mass of the star is subordinate and we can safely assume $N_2 \ll N_1$. Each one of the curves eventually lead towards the single scalar limit when $\Phi_2(0)$ grows larger. This behavior confirms the analytical approximation of the single scalar limits to determine the nonlinear and linear regimes done in section 2.6.

D Transitioning from Φ_1 to Φ_2 in the Nonlinear Regime

We numerically verify that in the nonlinear regime, the transition between ϕ_1 dominating to ϕ_2 dominating still happens as expected. As seen in Section 2.6, a two scalar hierarchy $m_1 < m_2$ interpolates two scenarios where Φ_1 dominates the system ($N_1 \gg N_2$) and that where Φ_2 dominates ($N_2 \gg N_1$.) We verify that this transitioning behavior still persists in the nonlinear regime.

One observes that when one scalar has a stable nonlinear self-interaction (e.g. $+\phi^4$), and the other unstable self-interaction (e.g. $-\phi^4$), once the system transitions from the unstable scalar dominating to the stable scalar dominating, it is then stabilized, and vice versa. This can be seen in Fig. 13. Another way of seeing this transitioning effect is through a less drastic setup, with $\lambda_1, \lambda_2 > 0$ but have different values. The $C - M$ curve has different shape if Φ_1 or Φ_2 forms BEC

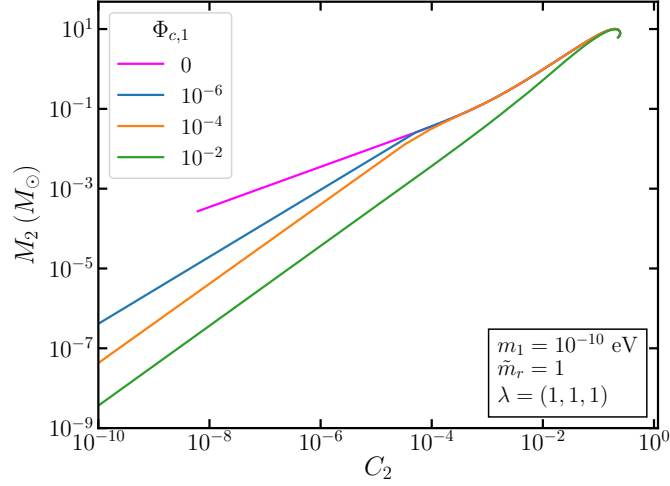


Figure 12: The changes to a single scalar BEC profile due to the existence of another scalar with varying central density. The mass versus compactness only taking into consideration the contribution from Φ_2 . The single scalar limit is given by the blue curve. The other curves at scanning over $\Phi_2(0)$ at different fixed values of $\Phi_1(0)$.

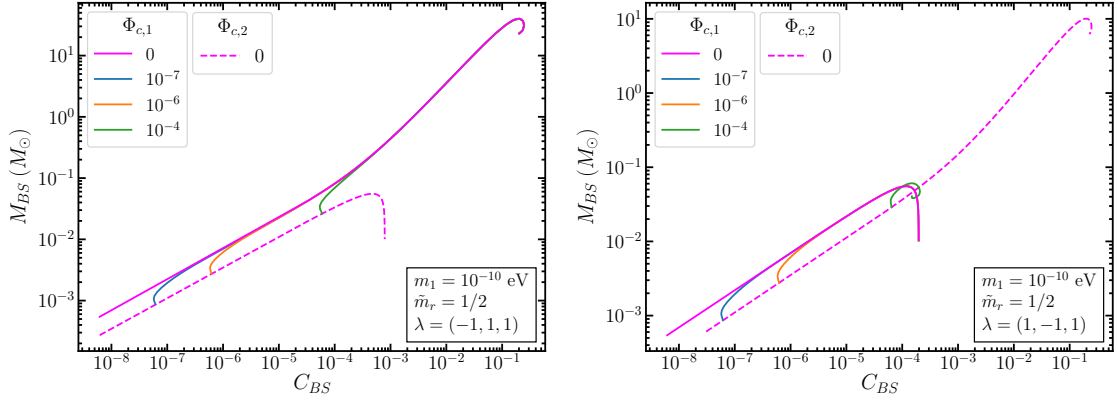


Figure 13: The total mass vs compactness for various values of $\Phi_1(0)$ and $\Phi_2(0)$, with $\lambda_1 = -1$, $\lambda_2 = 1$ (left) and $\lambda_1 = 1$, $\lambda_2 = -1$ (right). All solid curves are generated by scanning over $\Phi_2(0)$ and fixing $\Phi_1(0)$ at labeled values, while the dashed curve is setting $\Phi_2(0)$ to zero and scanning over $\Phi_1(0)$.

alone. In the two scalar system, by arranging $\Phi_1(0)$ and $\Phi_2(0)$ carefully, one can get any point in between the two curves shown as the shaded region in Fig. 14.

References

- [1] Steven Weinberg. A New Light Boson? *Phys. Rev. Lett.*, 40:223–226, 1978.
- [2] Frank Wilczek. Problem of Strong P and T Invariance in the Presence of Instantons. *Phys. Rev. Lett.*, 40:279–282, 1978.

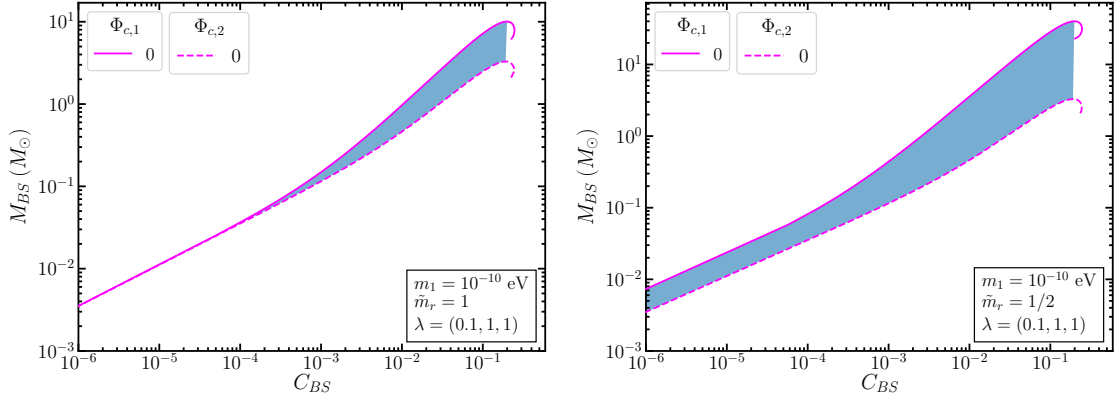


Figure 14: The mass profile of the BEC with $\lambda_1 = 0.1$, $\lambda_2 = 1$, and $\lambda_{12} = 1$. The mass ratio between the two scalars is $\tilde{m}_r = 1$ in the left figure and $\tilde{m}_r = 1/2$ in the right figure. The shaded region is the region a stable BEC system can form.

- [3] Peter Svrcek and Edward Witten. Axions In String Theory. *JHEP*, 06:051, 2006.
- [4] Asimina Arvanitaki, Savas Dimopoulos, Sergei Dubovsky, Nemanja Kaloper, and John March-Russell. String Axiverse. *Phys. Rev. D*, 81:123530, 2010.
- [5] Michele Cicoli, Mark Goodsell, and Andreas Ringwald. The type IIB string axiverse and its low-energy phenomenology. *JHEP*, 10:146, 2012.
- [6] Bobby Samir Acharya, Konstantin Bobkov, and Piyush Kumar. An M Theory Solution to the Strong CP Problem and Constraints on the Axiverse. *JHEP*, 11:105, 2010.
- [7] D.F. Jackson Kimball et al. Overview of the Cosmic Axion Spin Precession Experiment (CASPER). *Springer Proc. Phys.*, 245:105–121, 2020.
- [8] Antoine Garcon et al. Constraints on bosonic dark matter from ultralow-field nuclear magnetic resonance. 2 2019.
- [9] Jonathan L. Ouellet et al. First Results from ABRACADABRA-10 cm: A Search for Sub- μeV Axion Dark Matter. *Phys. Rev. Lett.*, 122(12):121802, 2019.
- [10] Itay M. Bloch, Yonit Hochberg, Eric Kuflik, and Tomer Volansky. Axion-like Relics: New Constraints from Old Comagnetometer Data. *JHEP*, 01:167, 2020.
- [11] Peter W. Graham, Selcuk Haciomeroglu, David E. Kaplan, Zhanibek Omarov, Surjeet Rajendran, and Yannis K. Semertzidis. Storage Ring Probes of Dark Matter and Dark Energy. 5 2020.
- [12] JiJi Fan. Ultralight Repulsive Dark Matter and BEC. *Phys. Dark Univ.*, 14:84–94, 2016.
- [13] M. Colpi, S. L. Shapiro, and I. Wasserman. Boson Stars: Gravitational Equilibria of Selfinteracting Scalar Fields. *Phys. Rev. Lett.*, 57:2485–2488, 1986.
- [14] Lam Hui, Jeremiah P. Ostriker, Scott Tremaine, and Edward Witten. Ultralight scalars as cosmological dark matter. *Phys. Rev. D*, 95(4):043541, 2017.
- [15] Hsi-Yu Schive, Tzihong Chiueh, and Tom Broadhurst. Cosmic Structure as the Quantum Interference of a Coherent Dark Wave. *Nature Phys.*, 10:496–499, 2014.
- [16] Hsi-Yu Schive, Ming-Hsuan Liao, Tak-Pong Woo, Shing-Kwong Wong, Tzihong Chiueh, Tom

- Broadhurst, and W.-Y. Pauchy Hwang. Understanding the Core-Halo Relation of Quantum Wave Dark Matter from 3D Simulations. *Phys. Rev. Lett.*, 113(26):261302, 2014.
- [17] Bodo Schwabe, Jens C. Niemeyer, and Jan F. Engels. Simulations of solitonic core mergers in ultralight axion dark matter cosmologies. *Phys. Rev. D*, 94(4):043513, 2016.
- [18] Jan Veltmaat and Jens C. Niemeyer. Cosmological particle-in-cell simulations with ultralight axion dark matter. *Phys. Rev. D*, 94(12):123523, 2016.
- [19] Philip Mocz, Mark Vogelsberger, Victor H. Robles, Jesús Zavala, Michael Boylan-Kolchin, Anastasia Fialkov, and Lars Hernquist. Galaxy formation with BECDM – I. Turbulence and relaxation of idealized haloes. *Mon. Not. Roy. Astron. Soc.*, 471(4):4559–4570, 2017.
- [20] Nicola C. Amorisco and A. Loeb. First constraints on Fuzzy Dark Matter from the dynamics of stellar streams in the Milky Way. 8 2018.
- [21] Eric Armengaud, Nathalie Palanque-Delabrouille, Christophe Yèche, David J. E. Marsh, and Julien Baur. Constraining the mass of light bosonic dark matter using SDSS Lyman-alpha forest. *Monthly Notices of the Royal Astronomical Society*, 471(4):4606–4614, 07 2017.
- [22] Katelin Schutz. Subhalo mass function and ultralight bosonic dark matter. *Phys. Rev. D*, 101(12):123026, 2020.
- [23] Nitsan Bar, Diego Blas, Kfir Blum, and Sergey Sibiryakov. Galactic rotation curves versus ultralight dark matter: Implications of the soliton-host halo relation. *Phys. Rev. D*, 98(8):083027, 2018.
- [24] Heling Deng, Mark P. Hertzberg, Mohammad Hossein Namjoo, and Ali Masoumi. Can Light Dark Matter Solve the Core-Cusp Problem? *Phys. Rev. D*, 98(2):023513, 2018.
- [25] Kfir Blum, Emanuele Castorina, and Marko Simonović. Could Quasar Lensing Time Delays Hint to a Core Component in Halos, Instead of H_0 Tension? *Astrophys. J. Lett.*, 892(2):L27, 2020.
- [26] Gian F. Giudice, Matthew McCullough, and Alfredo Urbano. Hunting for Dark Particles with Gravitational Waves. *JCAP*, 1610(10):001, 2016.
- [27] Steven L. Liebling and Carlos Palenzuela. Dynamical Boson Stars. *Living Rev. Rel.*, 20(1):5, 2017.
- [28] Reid Larimore Guenther. *A Numerical Study of the Time Dependent Schroedinger Equation Coupled with Newtonian Gravity*. PhD thesis, THE UNIVERSITY OF TEXAS AT AUSTIN., January 1995.
- [29] Enrico D. Schiappacasse and Mark P. Hertzberg. Analysis of Dark Matter Axion Clumps with Spherical Symmetry. *JCAP*, 01:037, 2018. [Erratum: *JCAP* 03, E01 (2018)].
- [30] Pierre-Henri Chavanis. Mass-radius relation of Newtonian self-gravitating Bose-Einstein condensates with short-range interactions: I. Analytical results. *Phys. Rev. D*, 84:043531, 2011.
- [31] P.H. Chavanis and L. Delfini. Mass-radius relation of Newtonian self-gravitating Bose-Einstein condensates with short-range interactions: II. Numerical results. *Phys. Rev. D*, 84:043532, 2011.
- [32] Luca Visinelli, Sebastian Baum, Javier Redondo, Katherine Freese, and Frank Wilczek. Dilute and dense axion stars. *Phys. Lett.*, B777:64–72, 2018.
- [33] Joshua Eby, Kyohei Mukaida, Masahiro Takimoto, L.C.R. Wijewardhana, and Masaki Yamada. Classical nonrelativistic effective field theory and the role of gravitational interactions. *Phys. Rev. D*, 99(12):123503, 2019.
- [34] Joshua Eby, Peter Suranyi, and L.C.R. Wijewardhana. Expansion in Higher Harmonics of Boson Stars using a Generalized Ruffini-Bonazzola Approach, Part 1: Bound States. *JCAP*, 04:038, 2018.

- [35] Joshua Eby, Madelyn Leembruggen, Lauren Street, Peter Suranyi, and L.C.R. Wijewardhana. Approximation methods in the study of boson stars. *Phys. Rev. D*, 98(12):123013, 2018.
- [36] Joshua Eby, Peter Suranyi, and L.C.R. Wijewardhana. The Lifetime of Axion Stars. *Mod. Phys. Lett. A*, 31(15):1650090, 2016.
- [37] Joshua Eby, Madelyn Leembruggen, Peter Suranyi, and L.C.R. Wijewardhana. Collapse of Axion Stars. *JHEP*, 12:066, 2016.
- [38] Marcelo Gleiser. Stability of boson stars. *Phys. Rev. D*, 38:2376–2385, Oct 1988.
- [39] Mark P. Hertzberg, Fabrizio Rompineve, and Jessie Yang. Decay of Boson Stars with Application to Glueballs and Other Real Scalars. 10 2020.
- [40] Djuna Croon, Jiji Fan, and Chen Sun. Boson Star from Repulsive Light Scalars and Gravitational Waves. *JCAP*, 1904(04):008, 2019.
- [41] A. Bernal, J. Barranco, D. Alic, and C. Palenzuela. Multistate boson stars. *Physical Review D*, 81(4), Feb 2010.
- [42] Felix Kling, Arvind Rajaraman, and Freida Liz Rivera. New Solutions for Rotating Boson Stars. 10 2020.
- [43] Kfir Blum, Raffaele Tito D’Agnolo, Mariangela Lisanti, and Benjamin R. Safdi. Constraining Axion Dark Matter with Big Bang Nucleosynthesis. *Phys. Lett. B*, 737:30–33, 2014.
- [44] Nitsan Bar, Kfir Blum, Joshua Eby, and Ryosuke Sato. Ultralight dark matter in disk galaxies. *Phys. Rev. D*, 99(10):103020, 2019.
- [45] Miguel Bezares and Carlos Palenzuela. Gravitational Waves from Dark Boson Star binary mergers. *Class. Quant. Grav.*, 35(23):234002, 2018.
- [46] Thomas Helfer, Eugene A. Lim, Marcos A. G. Garcia, and Mustafa A. Amin. Gravitational Wave Emission from Collisions of Compact Scalar Solitons. *Phys. Rev. D*, 99(4):044046, 2019.
- [47] P. S. Bhupal Dev, Manfred Lindner, and Sebastian Ohmer. Gravitational waves as a new probe of Bose–Einstein condensate Dark Matter. *Phys. Lett. B*, 773:219–224, 2017.
- [48] Mark P. Hertzberg and Enrico D. Schiappacasse. Dark Matter Axion Clump Resonance of Photons. *JCAP*, 11:004, 2018.
- [49] Mark P. Hertzberg, Yao Li, and Enrico D. Schiappacasse. Merger of Dark Matter Axion Clumps and Resonant Photon Emission. *JCAP*, 07:067, 2020.
- [50] Mustafa A. Amin and Zong-Gang Mou. Electromagnetic Bursts from Mergers of Oscillons in Axion-like Fields. 9 2020.
- [51] Huai-Ke Guo, Kuver Sinha, and Chen Sun. Probing Boson Stars with Extreme Mass Ratio Inspirals. *JCAP*, 09:032, 2019.
- [52] Anirudh Prabhu. Optical Lensing by Axion Stars: Observational Prospects with Radio Astrometry. 6 2020.
- [53] Djuna Croon, Marcelo Gleiser, Sonali Mohapatra, and Chen Sun. Gravitational Radiation Background from Boson Star Binaries. *Phys. Lett. B*, 783:158–162, 2018.
- [54] Lasha Berezhiani and Justin Khoury. Theory of dark matter superfluidity. *Phys. Rev.*, D92:103510, 2015.
- [55] Elisa G.M. Ferreira, Guilherme Franzmann, Justin Khoury, and Robert Brandenberger. Unified Superfluid Dark Sector. *JCAP*, 08:027, 2019.

- [56] Pierre-Henri Chavanis and Tiberiu Harko. Bose-Einstein Condensate general relativistic stars. *Phys. Rev. D*, 86:064011, 2012.
- [57] Jiajun Chen, Xiaolong Du, Erik W. Lentz, David J. E. Marsh, and Jens C. Niemeyer. New insights into the formation and growth of boson stars in dark matter halos. 11 2020.
- [58] Hoang Nhan Luu, S.-H. Henry Tye, and Tom Broadhurst. Multiple Ultralight Axionic Wave Dark Matter and Astronomical Structures. *Phys. Dark Univ.*, 30:100636, 2020.
- [59] Joshua Eby, Lauren Street, Peter Suranyi, L.C. R. Wijewardhana, and Madelyn Leembruggen. Galactic Condensates composed of Multiple Axion Species. 2 2020.
- [60] Nahomi Kan and Kiyoshi Shiraishi. A Newtonian Analysis of Multi-scalar Boson Stars with Large Self-couplings. *Phys. Rev. D*, 96(10):103009, 2017.
- [61] Yves Brihaye and Betti Hartmann. Interacting Q-balls. *Nonlinearity*, 21:1937, 2008.
- [62] Yves Brihaye and Betti Hartmann. Angularly excited and interacting boson stars and Q-balls. *Phys. Rev. D*, 79:064013, 2009.
- [63] Yves Brihaye, Thierry Caebergs, Betti Hartmann, and Momchil Minkov. Symmetry breaking in (gravitating) scalar field models describing interacting boson stars and Q-balls. *Phys. Rev. D*, 80:064014, 2009.
- [64] Davi C. Rodrigues, Antonino del Popolo, Valerio Marra, and Paulo L. C. de Oliveira. Evidence against cuspy dark matter haloes in large galaxies. *Mon. Not. Roy. Astron. Soc.*, 470(2):2410–2426, 2017.
- [65] William H. Press, Saul A. Teukolsky, William T. Vetterling, and Brian P. Flannery. *Numerical Recipes 3rd Edition: The Art of Scientific Computing*. Cambridge University Press, New York, NY, USA, 3 edition, 2007.
- [66] Ian Low, Witold Skiba, and David Tucker-Smith. Little Higgses from an antisymmetric condensate. *Phys. Rev. D*, 66:072001, 2002.
- [67] F. Donato, G. Gentile, P. Salucci, C. Frigerio Martins, M. I. Wilkinson, G. Gilmore, E. K. Grebel, A. Koch, and R. Wyse. A constant dark matter halo surface density in galaxies. *Mon. Not. Roy. Astron. Soc.*, 397:1169–1176, 2009.
- [68] Paolo Salucci. The distribution of dark matter in galaxies. *Astron. Astrophys. Rev.*, 27(1):2, 2019.
- [69] Wayne Hu, Rennan Barkana, and Andrei Gruzinov. Cold and fuzzy dark matter. *Phys. Rev. Lett.*, 85:1158–1161, 2000.
- [70] Vid Iršič, Matteo Viel, Martin G. Haehnelt, James S. Bolton, and George D. Becker. First constraints on fuzzy dark matter from Lyman- α forest data and hydrodynamical simulations. *Phys. Rev. Lett.*, 119(3):031302, 2017.
- [71] Matteo Nori, Riccardo Murgia, Vid Iršič, Marco Baldi, and Matteo Viel. Lyman α forest and non-linear structure characterization in Fuzzy Dark Matter cosmologies. *Mon. Not. Roy. Astron. Soc.*, 482(3):3227–3243, 2019.
- [72] Asimina Arvanitaki, Savas Dimopoulos, Marios Galanis, Luis Lehner, Jedidiah O. Thompson, and Ken Van Tilburg. Large-misalignment mechanism for the formation of compact axion structures: Signatures from the QCD axion to fuzzy dark matter. *Phys. Rev. D*, 101(8):083014, 2020.
- [73] Yang Bai, Andrew J. Long, and Sida Lu. Dark Quark Nuggets. *Phys. Rev. D*, 99(5):055047, 2019.
- [74] Eric Braaten, Abhishek Mohapatra, and Hong Zhang. Dense Axion Stars. *Phys. Rev. Lett.*, 117(12):121801, 2016.

- [75] Sebastian Khan, Sascha Husa, Mark Hannam, Frank Ohme, Michael Pürrer, Xisco Jiménez Forteza, and Alejandro Bohé. Frequency-domain gravitational waves from nonprecessing black-hole binaries. II. A phenomenological model for the advanced detector era. *Phys. Rev. D*, 93(4):044007, 2016.
- [76] Lisa Barsotti, Peter Fritschel, Matthew Evans, and Slawomir Gras. LIGO Document T1800044-v5. LIGO Document T1800044-v5, <https://dcc.ligo.org/LIGO-T1800044/public>.
- [77] T. Akutsu et al. Overview of KAGRA: Detector design and construction history. 5 2020.
- [78] R. Abbott et al. GW190521: A Binary Black Hole Merger with a Total Mass of $150 M_{\odot}$. *Phys. Rev. Lett.*, 125(10):101102, 2020.
- [79] R. Abbott et al. Properties and Astrophysical Implications of the $150 M_{\odot}$ Binary Black Hole Merger GW190521. *Astrophys. J.*, 900(1):L13, 2020.
- [80] Juan Calderón Bustillo, Nicolas Sanchis-Gual, Alejandro Torres-Forné, José A. Font, Avi Vajpeyi, Rory Smith, Carlos Herdeiro, Eugen Radu, and Samson H.W. Leong. The (ultra) light in the dark: A potential vector boson of 8.7×10^{-13} eV from GW190521. 9 2020.
- [81] N. Arkani-Hamed, A.G. Cohen, E. Katz, and A.E. Nelson. The Littlest Higgs. *JHEP*, 07:034, 2002.
- [82] N. Arkani-Hamed, A.G. Cohen, E. Katz, A.E. Nelson, T. Gregoire, and Jay G. Wacker. The Minimal moose for a little Higgs. *JHEP*, 08:021, 2002.
- [83] Martin Schmaltz and Jesse Thaler. Collective Quartics and Dangerous Singlets in Little Higgs. *JHEP*, 03:137, 2009.